

RESEARCH ARTICLE

10.1002/2015JB012698

Key Points:

- Tomography reveals structural variations in the Southeastern United States upper mantle
- Imaged velocity patterns can be interpreted as ongoing lithospheric foundering
- Tectonism and intraplate volcanism are due to tectonic inheritance and lithospheric foundering

Supporting Information:

- Supporting Information S1

Correspondence to:

C. B. Biryol,
biryol@live.unc.edu

Citation:

Biryol, C. B., L. S. Wagner, K. M. Fischer, and R. B. Hawman (2016), Relationship between observed upper mantle structures and recent tectonic activity across the Southeastern United States, *J. Geophys. Res. Solid Earth*, 121, doi:10.1002/2015JB012698.

Received 30 NOV 2015

Accepted 29 FEB 2016

Accepted article online 8 MAR 2016

Relationship between observed upper mantle structures and recent tectonic activity across the Southeastern United States

C. Berk Biryol¹, Lara S. Wagner², Karen M. Fischer³, and Robert B. Hawman⁴

¹Geological Sciences Department, University of North Carolina at Chapel Hill, Chapel Hill, North Carolina, USA, ²Department of Terrestrial Magnetism, Carnegie Institution for Science, Washington, District of Columbia, USA, ³Department of Earth, Environmental, and Planetary Sciences, Brown University, Providence, Rhode Island, USA, ⁴Department of Geology, University of Georgia, Athens, Georgia, USA

Abstract The lithospheric structure of the Southeastern United States is a product of earlier episodes of continental collision and breakup. The region is located in the interior of the North American Plate, away from active plate margins. However, there is ongoing tectonism in the region with multiple zones of seismicity, uplifting arches, and Cenozoic intraplate volcanism. The mechanisms controlling this activity and the state of stress remain enigmatic. Two important factors are plate strength and preexisting, inherited structures. Here we present new tomographic images of the upper mantle beneath the Southeastern United States, revealing large-scale structural variations in the upper mantle. Examples include the relatively thick lithospheric mantle of stable North America that abruptly thins beneath the Paleozoic Appalachian orogeny, and the slow upper mantle of the Proterozoic Reelfoot rift. Our results also indicate fast seismic velocity patterns that can be interpreted as ongoing lithospheric foundering. This provides a viable explanation for seismicity, uplifting, and young intraplate volcanism. We postulate that not only tectonic inheritance but also continuing lithospheric foundering may control the ongoing activity of the region long after it became a passive margin. Based on distinct variations in the geometry and thickness of the lithospheric mantle and foundered lithosphere, we propose that piecemeal delamination has occurred beneath the region throughout the Cenozoic, removing a significant amount of reworked/deformed mantle lithosphere. Ongoing lithospheric foundering beneath the eastern margin of stable North America explains significant variations in thickness of lithospheric mantle across the former Grenville deformation front.

1. Introduction

Detailed studies of tectonic plate boundaries have yielded a much-improved understanding of the mechanisms that control the deformation and evolution of plate margins. However, the processes controlling tectonic activity within plate interiors are poorly understood. Significant questions remain regarding the state of stress and the strength of the continental lithosphere away from plate boundaries. Various factors may contribute to these attributes including the thickness of the lithosphere and the presence of inherited structures from earlier tectonic episodes.

The Southeastern United States (SEUS) is an ideal location to investigate the evolution of plate interiors because of the diversity of its ongoing tectonism and the inherited structures it contains. The SEUS is the product of multiple episodes of tectonic accretion and rifting that have taken place since the Late Proterozoic (>1.0 Ga) [Cook *et al.*, 1979; Thomas, 2006; Hatcher, 2010], but it has not been near a plate boundary for over 150 Myr (Figure 1). Today, the SEUS is located over 1700 km away from the closest plate boundary, but it still comprises multiple zones of active seismicity, including a number of destructive earthquakes such as the 1886 Charleston, South Carolina (SC) earthquake ($M_w = 7.0$) [Johnston, 1996; Bartholomew *et al.*, 2002] (Figure 1) and the 2011 Mineral, Virginia (VA) earthquake ($M_w = 5.8$) [Wolin *et al.*, 2012]. In addition to significant intraplate seismicity, various geomorphological observations point to ongoing Cenozoic epeirogeny, including evidence for recent uplift of the ancient Appalachian orogen (Figure 1) [Spotila *et al.*, 2004; Gallen *et al.*, 2013; Liu, 2014], northwestward migration of the Blue Ridge [Willett *et al.*, 2014] and the presence of recently uplifted coastal arches and scarps [Winker and Howard, 1977; Rowley *et al.*, 2013].

In this study, we identify possible connections between upper mantle attributes of the SEUS and observed intraplate tectonism. Our finite-frequency teleseismic body wave tomography provides improved images

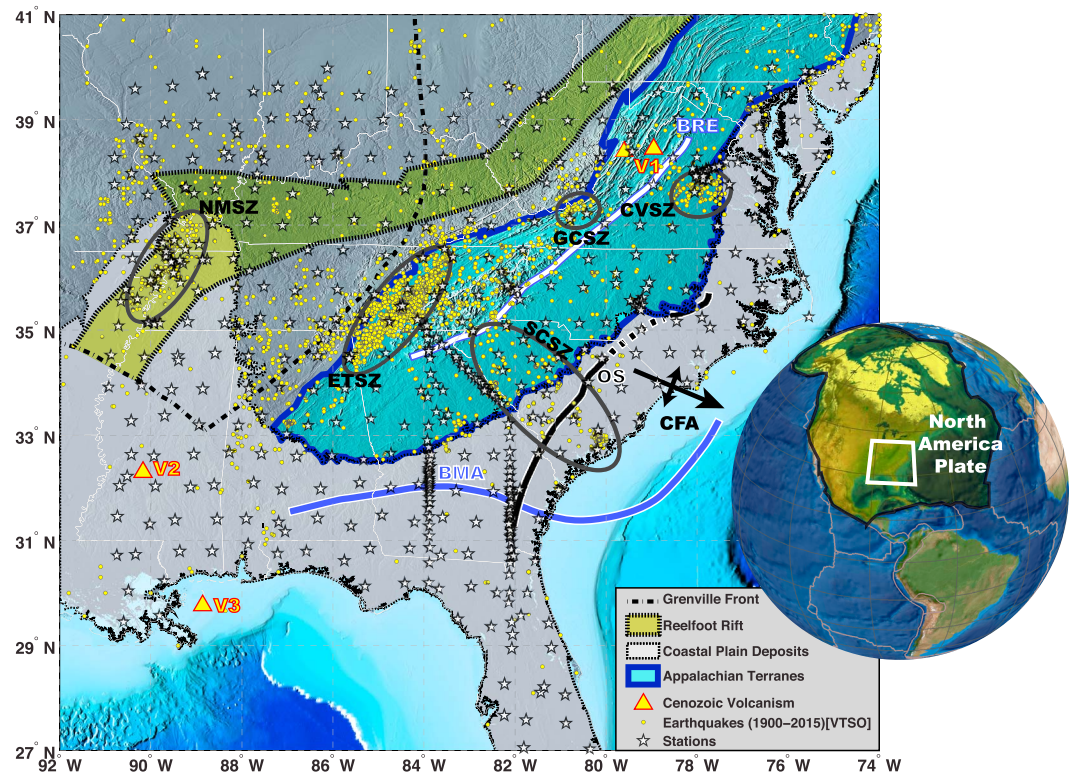


Figure 1. Map of the study area showing various tectonic attributes of the Southeastern United States. BMA = Brunswick Magnetic Anomaly, BRE = Blue Ridge Escarpment, CFA = Cape Fear Arch, OS = Orangeburg Scarp, ETSZ = Eastern Tennessee Seismic Zone, NMSZ = New Madrid Seismic Zone, GCSZ = Giles County Seismic Zone, SCSZ = South Carolina Seismic Zone, CVSZ = Central Virginia Seismic Zone, V1 = Eocene Virginia Volcanics, V2 = Jackson, Mississippi Volcanism, V3 = Offshore Louisiana Volcanism. Seismicity is from the Virginia Tech Seismological Observatory catalog (1900–2014).

of the upper mantle by using data from both SESAME (Southeastern Suture of the Appalachian Margin Experiment) [Parker *et al.*, 2013; MacDougall *et al.*, 2015; Parker *et al.*, 2015] and the EarthScope Transportable Array. We identify major upper mantle structures that provide insights into the ongoing and past processes governing the SEUS.

2. Tectonic Setting

In the SEUS, the oldest known episode of continental accretion is associated with the Grenville orogeny [Thomas, 1982; Denison *et al.*, 1987]. This episode marks the assembly of the supercontinent Rodinia (~1.1 Ga) that rifted at ~570 Ma, leading to the opening of the Iapetus Ocean [Rogers and Santosh, 2002; Rogers and Santosh, 2003; Thomas, 2006]. The western deformation front of the Grenville orogeny, the Grenville front (GF), roughly marks the exposed boundary between the old stable core of North America and the SEUS continental margin [Thomas, 1982; Culotta *et al.*, 1990]. The breakup of Rodinia resulted in the formation of aulacogens within the ancient Grenville terrane. One of the most prominent of these is the Reelfoot rift (RFR) (Figure 1) [Burke and Dewey, 1973; Hildenbrand and Hendricks, 1995].

Following Iapetan rifting, several orogenic episodes resulted in the accretion of a suite of terranes along what is now the SEUS, ending with the Alleghanian orogeny (330 Ma). This final orogenic episode, caused by the collision of Laurentia and Gondwana, completed the assembly of the supercontinent Pangea [Iverson and Smithson, 1983; Rankin *et al.*, 1991]. It is particularly important as it is the most recent phase of mountain building in the region. A number of seismic studies indicate the existence of a shallow, low-angle, continuous regional reflector, that has been interpreted as an underlying detachment, separating Grenville/Laurentian basement below from allochthonous blocks that make up the accreted terranes of the SEUS passive margin above (Figure 1) [Cook *et al.*, 1979; Harris and Bayer, 1979; Hibbard, 2000; Cook and Vasudevan, 2006; Hawman, 2008; Hawman *et al.*, 2012; Hibbard *et al.*, 2012]. The eastward extent of this detachment and the westward

extent of the Appalachian terranes at depth remain unclear. While most agree that the bounding Alleghanian suture at depth is located well eastward of the GF, there is disagreement about whether Grenville basement ends beneath the central Carolinas [Hibbard, 2000] or extends farther east beneath the coastal plains [Cook and Vasudevan, 2006] (Figure 1).

In addition to the extensive deformation across the Appalachians, the collision between Laurentia and Gondwana resulted in the addition of the Suwannee terrane that comprises much of Florida and southern Georgia [Hatcher, 2010; Thomas, 2010; Mueller et al., 2014]. This terrane has significantly different deformational attributes, lithostratigraphy, fossil assemblages, and geochemical signatures than Laurentia [Mueller et al., 2014]. Based on these differences, the Suwannee Suture (SWS), which is the continuation of the Alleghanian suture to the south, is believed to be coincident with the regionally extensive, east-west trending Brunswick Magnetic Anomaly (BMA in Figure 1) [Higgins and Zietz, 1983; Williams and Hatcher, 1983; Mueller et al., 2014].

The subsequent rifting of Pangea (~200 Ma) led to widespread volcanism and the opening of Atlantic Ocean basin (190 Ma) [Marzoli et al., 1999; Blackburn et al., 2013], after which North American continental crust was gradually isolated by seafloor spreading and the SEUS became the passive margin we have today [Thomas, 2006].

At present, the SEUS is characterized by unusual patterns of passive margin seismicity, ongoing epeirogeny, and relatively young intraplate volcanism. Their origins, factors that control their spatial and temporal occurrence, and how they have evolved over time are poorly understood. However, some studies indicate that this activity could be associated with the reactivation of inherited, older structures of the region such as the Reelfoot rift (RFR) [Ervin and McGinnis, 1975; Pollitz et al., 2001; Van Arsdale and Cox, 2007; Pollitz and Mooney, 2014].

The seismicity of the region is particularly significant, as the SEUS is among the most seismically "active" passive margins in the world (Figure 1). The New Madrid Seismic Zone (NMSZ) and the Eastern Tennessee Seismic zone (ETSZ) are the largest and most active seismogenic zones of the region. The NMSZ is located within the bounds of the RFR, and it is usually associated with the reactivation of inherited old shear zones within the rift [Hildenbrand and Hendricks, 1995; Pollitz and Mooney, 2014]. It is not clear why this zone is spatially limited to the northern part of the Mississippi Embayment [Newman et al., 1999; Tuttle et al., 2002]. The ETSZ is characterized by relatively high cumulative strain energy release along widely separated, reactivated shear zones of the crystalline Grenville basement [Powell et al., 1994; Wheeler, 1995; Vlahovic et al., 1998; Powell and Thomas, 2016]. However, it is not clear why the proposed old shear zones are better preserved here than elsewhere.

There are a number of other regions of increased seismicity across our study area. The cluster of seismicity located across South Carolina and northeastern Georgia comprises the South Carolina Seismic Zone (SCSZ, Figure 1). This region includes the devastating 1886 Charleston, SC earthquake. Studies indicate that the faults associated with this seismicity may also control the regional uplifting of coastal sediments [Rhea, 1989; Marple and Talwani, 1993; Bartholomew et al., 2002]. Farther north, the Central Virginia Seismic Zone (CVSZ, Figure 1) in north-central Virginia is characterized by a cluster of earthquakes. The CVSZ is also the site of the 23 August 2011 Mineral, VA earthquake ($M_w = 5.8$) [Wolin et al., 2012; Pratt et al., 2014]. The final prominent, densely clustered seismic zone of the region is the Giles County Seismic Zone (GCSZ, Figure 1) [Bollinger and Wheeler, 1983]. Similar to the ETSZ and NMSZ, the seismogenic zone of GCSZ is associated with the reactivation of normal faults in the old crystalline basement, formed during lapetan rifting [Wheeler, 1995].

Another poorly understood deformational attribute of the region is the relatively young episode of epeirogeny [Pazzaglia and Gardner, 1994], evidenced by local uplifts (arches), the presence of warped coastal scarps and escarpments, as well as the migration of knickpoints along river profiles. One of the most prominent coastal uplifts is the Cape Fear Arch (CFA, Figure 1) [Hersey et al., 1959; Soller, 1988]. This region, located at the state line between North Carolina and South Carolina, is characterized by a Pliocene (~3 Ma) basement uplift marked by an erosional surface [Hersey et al., 1959; Van De Plassche et al., 2014]. The mechanism behind this isolated uplift is not clear, but various proposed mechanisms suggest influence of mantle flow and lithospheric strength [Vogt, 1991; Pazzaglia and Gardner, 1994]. In addition to these local indicators, an upwarping of the originally flat, wave-cut coastal scarps indicates the uplift in the region [Winker and Howard, 1977].

An important example is the Pliocene Orangeburg Scarp (OS, Figure 1), which starts in southeastern Georgia and continues to the north paralleling the modern shoreline to central North Carolina [Huddleston, 1993]. Along the scarp, the coeval sedimentary deposits appear at different elevations, indicating post-Pliocene warping or tilting of the coastal plains of the SEUS [Winker and Howard, 1977; Huddleston, 1993; Bartholomew and Rich, 2013].

Farther west, another prominent morphologic feature with an ambiguous origin is the Blue Ridge Escarpment (BRE, Figure 1). This escarpment is 300–500 m high, with east facing steep slopes resembling those of active mountain ranges [Spotila *et al.*, 2004]. Recent work on knickpoint migration in rivers in the Blue Ridge mountains indicate changes in river incision rates due to external forces that could be climatic or uplift related [Gallen *et al.*, 2013; Miller *et al.*, 2013; Prince and Spotila, 2013]. Some of these studies favor uplift as the explanation for the observed knickpoint migration [Gallen *et al.*, 2013; Miller *et al.*, 2013]. It is possible that mantle density-controlled changes in dynamic support could be affecting the observed recent onset of tectonism and dynamics [Wagner *et al.*, 2012]. However, there are other possible explanations for the origin of the BRE, the related rejuvenation of Appalachian topography, and the migration of knickpoints. These include differential erosion and exhumation [Spotila *et al.*, 2004; Willett *et al.*, 2014] as well as flexural response to erosion [Pazzaglia and Gardner, 2000].

The contribution of the mantle to the geologic characteristics of the region is also evident in the postbreakup, intraplate volcanism in the region. A recent study by Mazza *et al.* [2014] has found evidence of 48 Ma volcanism in northwestern Virginia (V1, Figure 1). The geochemical signatures of the associated volcanic rocks indicate an uppermost mantle source for the magmas [Mazza *et al.*, 2014]. The existence of mantle-derived melts in this location is particularly surprising given that they formed in an orogen that had not been active for almost 330 Ma, and they formed in the absence of any known local failed rifts. This suggests more recent changes in the mantle that we can investigate using tomographic imaging.

3. Data and Methods

3.1. Data

We study the upper mantle structure of the SEUS using teleseismic *P* wave tomography. The data for our tomography are *P* wave relative travel times. We obtain these travel times using data from 514 stations belonging to various seismographic networks that operated in the region between 2010 and 2015 (Figure 1). These networks are the following: EarthScope Transportable Array [IRIS Transportable Array, 2003], ESVSME [Chiu, 2010], MAGIC [Long and Wiita, 2013], SCSN [University of South Carolina, 1987], CERI Southern Appalachian Seismic Network, GSN [Albuquerque Seismological Laboratory (ASL)/USGS, 1988], Lamont-Doherty Cooperative Seismographic Network, CEUSN [UC San Diego, 2013], Cooperative New Madrid Seismic Network, Penn State Network, PEPP-Indiana, USNSN [USGS National Earthquake Information Center (NEIC), 1990], OIINK [Pavlis and Gilbert, 2011], Pre-Hydrofracking Regional Assessment of Central Carolina Seismicity Network, PASEIS, Detection and location of nonvolcanic tremor in the New Madrid Seismic Zone Network [Langston and DeShon, 2009], Texas Brine Corporation Louisiana Seismic Network, Appalachian Seismic Transect (AST) [Wagner *et al.*, 2012], ENAM CSE, and the dense network of the Southeastern Suture of the Appalachian Margin Experiment (SESAME) [Fischer *et al.*, 2010] which comprised 85 stations deployed between July 2010 and May 2014.

We measure travel time residuals of direct *P* phases from 753 teleseismic earthquakes that occurred between 2010 and 2015 (Figure 2a). These events have magnitudes (M_w) greater than 5.5 at distances of 30° to 90°. In addition to direct *P* phases, we also obtain arrival times of steeply incident PKPdf phases from 23 earthquakes located within the 155° to 180° distance range (Figure 2a). We use the Multi-Channel Cross-Correlation technique of Pavlis and Vernon [2010] for picking the arrival times of direct *P* and PKPdf phases on the vertical components of the broadband seismograms. Travel time residuals are calculated with respect to IASP91 [Kennett *et al.*, 1995]. We obtain a total of 117,812 direct *P* and 2287 PKPdf travel time residuals. We calculate the relative travel time residuals by demeaning the residuals for each event.

The seismic signals from earthquakes observed on seismograms have finite-frequency spectra. Due to this finite-frequency content (finite bandwidth), the arrival times of these signals are sensitive to the seismic speed variations of the media around the seismic raypath [Woodward, 1992; Marquering *et al.*, 1999; Dahlen *et al.*, 2000]. Different frequency bands are sensitive to the velocity structure of different volumes

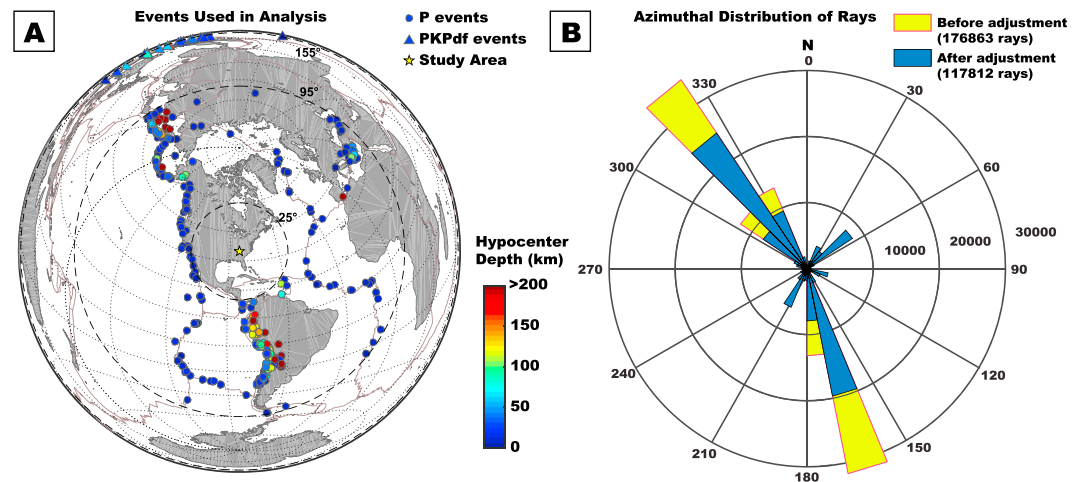


Figure 2. Summary of data coverage. (a) Map of the teleseismic events between 2010 and 2015 that we used in this study. Hypocenter depths for events are color coded. (b) Azimuthal coverage of measured arrivals before and after azimuthal adjustment for directional bias.

around the raypath. In this study we take advantage of this finite-frequency attribute of the seismic arrivals by repeating our picking procedure over three frequency bands. These bands are 0.2–0.8 Hz, 0.1–0.4 Hz, and 0.04–0.16 Hz and constitute 33%, 39%, and 28% of the data set, respectively. Data of individual frequency bands have RMS values between 0.36 and 0.40 s, with an overall data set RMS of 0.39 s.

We make several adjustments to the travel time residuals before incorporating them in the tomographic inversion. In order to reduce directional bias, we eliminate outlier relative residual travel times from heavily sampled back azimuths that are more than one standard deviation from the mean, yielding a less biased distribution (Figure 2b). Even though the back azimuthal coverage of the data set is still not uniform, the incidence angles for the teleseismic arrivals are subvertical and hence less likely to introduce a major bias in lateral directions compared to bias due to the steep incidence angles of sampling rays that limit the number of crossing raypaths. We also correct the observed relative travel time residuals to account for crustal heterogeneities using ray theory [Schmandt and Humphreys, 2010]. In order to calculate correction times, we incorporate crustal thicknesses and crustal P wave velocity estimates obtained from several seismic studies in the region [Cook *et al.*, 1979; Cook and Vasudevan, 2006; Hawman, 2008; French *et al.*, 2009; Abt *et al.*, 2010; Moidaki *et al.*, 2010; Hawman *et al.*, 2012; Wagner *et al.*, 2012; Parker *et al.*, 2013]. We also incorporate S wave velocity estimates from recent surface wave tomography studies [Pollitz and Mooney, 2014] in conjunction with crustal V_p/V_s estimates from various receiver function studies [French *et al.*, 2009; Abt *et al.*, 2010; Moidaki *et al.*, 2010; Hawman *et al.*, 2012; Wagner *et al.*, 2012; Parker *et al.*, 2013] in order to obtain crustal P wave velocity estimates for calculating the correction times (see Figure S1 in the supporting information). Even though these corrections are important, our results without these crustal corrections yielded a similar overall layout of the velocity perturbations indicating our resultant model does not depend significantly on the assumed crustal structure (see Figure S2 in the supporting information).

3.2. Methods and Model Parameterization

We use the tomographic inversion algorithm of Schmandt and Humphreys [2010] that incorporates the calculation of approximate 3-D sensitivity kernels for each observation of relative travel time residual in the associated frequency band. The algorithm uses the Born theoretical “Banana-Doughnut” kernel approximation of Dahlen *et al.* [2000] to calculate travel time sensitivities of arrivals to velocity perturbations for a given frequency band within the associated Fresnel zone. Even though this approximation is based on ray theory, it successfully circumvents the limitations of infinite frequency approximation [Dahlen *et al.*, 2000; Nolet *et al.*, 2005].

Additional constraints are applied to the inversion. The smoothing constraint accounts for geometric ray location uncertainty normal to the raypath and along the ray as well as probable sources of error due to noise in the data [Saltzer and Humphreys, 1997]. Gradient and norm damping is also applied to yield the least

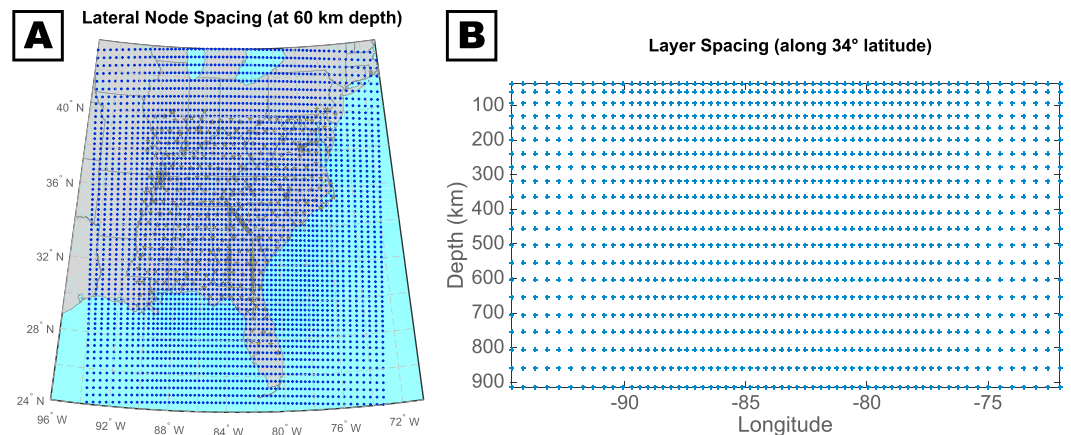


Figure 3. (a) Map of tomographic grid showing lateral spacing of nodes in our model. (b) Cross section through the center of the model space showing vertical node spacing.

possible model trade-off along the ray paths as well as to ensure a minimum length solution satisfying the travel time observations while strongly downweighting poorly sampled anomalies in the model [Schmandt and Humphreys, 2010]. Trade-off analyses between Euclidian model norm and norm misfit are performed in order to obtain optimal damping and smoothing values (see Figure S3 in the supporting information). These tests show insignificant variations in resultant model and in variance reductions with slight increases in damping and smoothing parameters, providing a stable final solution. The inverse problem is solved using the LSQR algorithm of Paige and Saunders [1982]. This algorithm targets minimization of the least squares misfit between calculated and observed data in an iterative sequence. We obtain a final RMS of 0.1 s for the residual misfit with the optimized values of damping (5) and smoothing (3), giving a variance reduction of 90%.

In addition, we calculate station and event terms that account for seismic velocity heterogeneities that lie outside the target volume. Although we have corrected the observed data for crustal structure, we also calculate individual station terms that account for small-scale local variations that are not a part of the applied crustal corrections. The RMS of the station terms is 0.08 s, which is small compared to the RMS of the entire inverted data set (0.45). Strong damping is also applied to station terms in order to avoid absorption of mantle structures in these terms. Event terms are also calculated to represent adjustment of the mean travel time for the set of stations that recorded each event. This is particularly important, as the data set is made of station sets that operate in different periods of time, located at different geographic settings, and record different events. This can introduce shifts in calculated mean travel time residuals between each group of stations sampling separate portions of the modeled domain. The event terms account for such shifts in mean travel time residuals and mean velocity structure at different parts of the study area [Schmandt and Humphreys, 2010].

Our study area roughly covers a 1500 km-by-1500 km region (Figure 3). The average station spacing in this region is 50 km (Figure 3a). This wide and dense coverage enables us to parameterize the region with an irregularly spaced 3-D rectangular grid that starts at 36 km depth and extends down to 915 km. In our parameterized model, lateral node spacing is 30 km beneath the region covered by stations, and this gradually expands outward to 45 km away from the center. The vertical spacing between layers of nodes expands from 35 km at the top to 55 km toward the bottom of the model (Figure 3b). Such a dilation in vertical node spacing with depth accounts for relatively sparser sampling of deeper layers and consequent reduction in resolution. With this geometry, our parameterized model has 82,026 nodes in 21 layers, each constituting a grid of 63 latitudinal and 62 longitudinal nodes.

In order to estimate the sampling of the model space, we compute sampling quality maps (hit quality maps) for each layer of the model (Figure 4). The qualities assigned to the nodes depend on the number of times the node is sampled as well as variability in back azimuthal distribution and incidence angles of the rays sampling the node. These values are normalized by the maximum possible hit quality that could be achieved for a model node (see supporting information for a detailed description of hit quality calculation procedure)

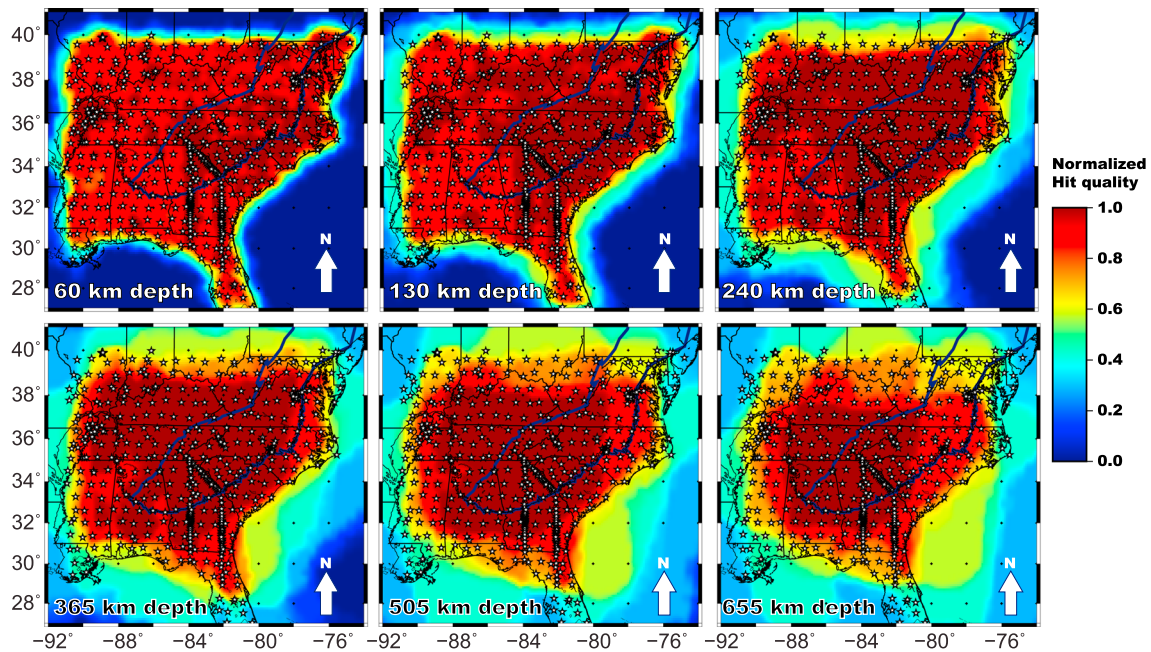


Figure 4. Normalized node hit quality maps for individual layers, showing the sampling of the model space at various depths. A quality of 1 indicates perfect sampling while a quality of 0 indicates no sampling of the associated nodes.

[Schmandt and Humphreys, 2010]. Better-sampled nodes (hit quality = 1) have more rays that sample them, and these rays are azimuthally well distributed. At the top of the model (36 km depth) better sampling is restricted to the nodes located directly beneath each station due to the near-vertical incidence angle of arrivals. This reduces the overall resolution in this layer. Consequently, we describe and interpret our results starting from the layer below the top (60 km depth). We also mask out those sections of our tomographic model that have hit qualities of less than 0.5 and only interpret the sections that have higher hit qualities.

4. Results

The resulting tomographic model reveals multiple regions of fast- and slow-velocity perturbations (Figure 5). Overall, the well-resolved fast and slow regions occupy similar quantities of nodes in the model space but display significant variability in distribution and amplitudes. Hence, we divide these anomalies into groups and describe the attributes of those most prominent in our model.

Major fast anomalies can be categorized into two subsets. One subset constitutes shallower, more horizontal anomalies, while the other is associated with deeper and steeply dipping anomalies. Among the first subset, the shallow flat-lying anomaly located at the northwest quadrant of the model (F1) appears to be 200–250 km thick (Figures 5a, 5b, and 6, cross section 4). F1 constitutes one of the fastest portions of our model with variations in seismic velocity perturbation amplitudes (see Table 1). F1 is located to the west of another flat, shallow anomaly, F2 (Figures 5a, 5b, and 6, cross section 5). The thickness of F2 is significantly less than F1 (less than 100–150 km). Compared to F1, F2 is slightly slower. As with anomaly F1, the strength of this anomaly varies across the region but is consistently fast (Table 1, Figures 5a and 5b between latitudes 36° and 38°, Figure 6, cross section 4). The geometry of F2 varies significantly, becoming narrower and thinner south of 37°N (Figures 5a, 5b, and 6, cross sections 4 and 6).

Fast anomalies in the second group are located at depths greater than 200 km. A narrow anomaly, F3, is located between 32° and 38°N (Figures 5d and 6, cross sections 2 and 4–6). F3 does not cover as large a portion of the model space as the shallower F1 and F2 anomalies (Table 1). It has an eastward dip of $\sim 45^\circ$ between 200 and 410 km depths (Figure 6, cross sections 4–6). Below F3 lies F4, located in the mantle transition zone (MTZ). This anomaly is less north-south elongated and does not have a discernable dip. It is substantially thicker than F3, filling much of the transition zone within its rectangular footprint.

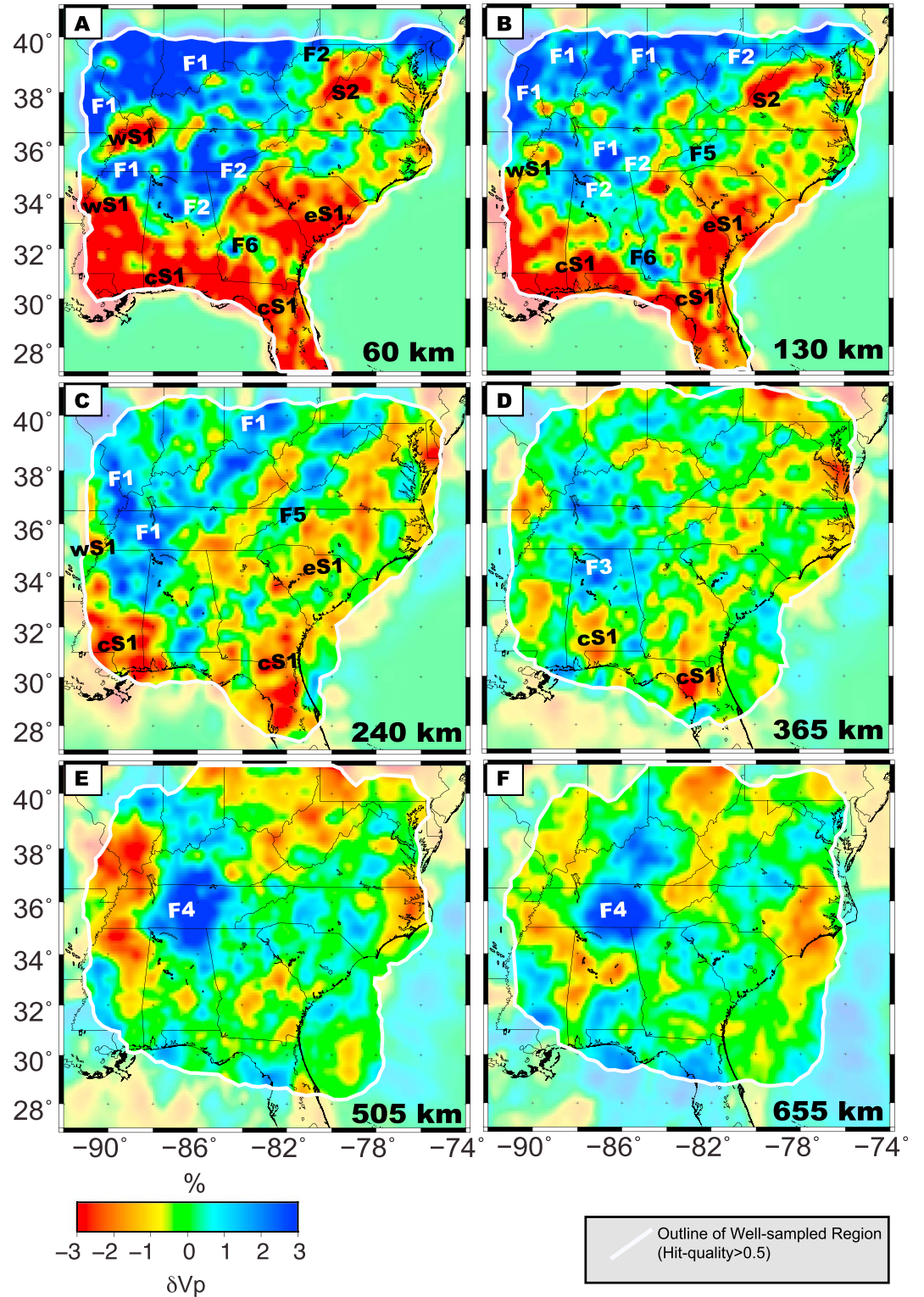


Figure 5. Tomographic model showing *P* wave velocity perturbation at various depth slices. Anomalies are labeled at corresponding depths (see text for description). Portions with subideal sampling are masked.

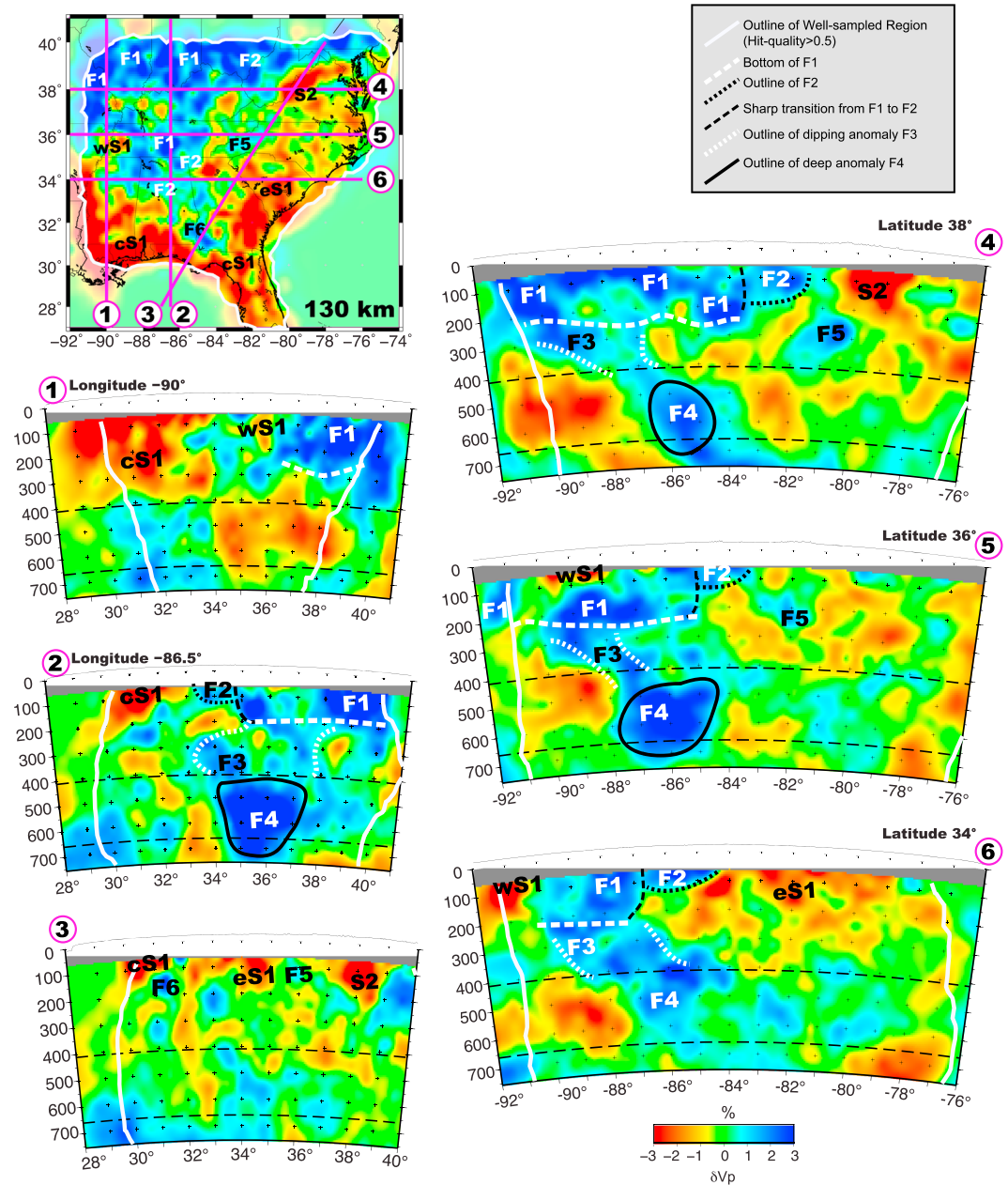


Figure 6. Tomographic model showing *P* wave velocity perturbation along various latitudinal and longitudinal profiles. Anomalies are labeled and outlined (see text for description). Top map shows the 130 km slice from the model together with the locations of the profiles.

(Figures 5e, 5f, and 6 cross section 2). F4 occupies a significant but smaller portion of the model space than other shallow F1 and F2 anomalies, but it constitutes the fastest part of our model (Table 1).

All of the major fast anomalies described above are physically adjacent to one another. Although F1 and F2 are part of a continuous anomaly, their boundary is defined by a clear variation in thickness. F2 is thinner and lies to the east, while F1 is thicker and lies in the central parts of the model. The transition between F1 and F2 roughly coincides with the location of Grenville front in the surface. This sharp transition is less clear in the north where F2 appears somewhat thicker. The sharp thickness variation aside, similar perturbation amplitudes, and their locations indicate a continuity of F1 into F2 from west to east (Figures 5a, 5b, and 6, cross sections 2 and 4–6). The tomographic images also show F3 as the deeper continuation of the shallower F1 and F2 (Figure 6, cross sections 2 and 4–6). In the deeper parts of the model, F3 and F4 appear to be in contact

Table 1. Summary of the Anomaly Attributes^a

Anomaly	Anomaly Attributes			
	Mean Perturbation (%)	Perturbation Standard Deviation (%)	Perturbation Maximum (%)	% of Model
F1	+1.8	1.2	9.4	10.8
F3	+1.4	0.8	4	2.2
F4	+2.2	1	5	4.6
F2	+1.6	1.1	6.3	4.5
F5	+1	0.7	3.4	0.3
F6	+1.2	0.9	3.4	0.1
cS1	-1.9	1.4	-7.3	11.2
eS1	-1.5	1.1	-7.6	13.1
Overall S1	-1.6	1.2	-7.6	24.3
S2	-1.6	1.2	-6	1.8

^aMean perturbation amplitudes, standard deviation of perturbation, maximum perturbation, and model space coverage of the anomalies are listed. The model space coverage is based on the number of model nodes with fast- or slow-velocity perturbations that make up each anomaly relative to the total number of the model nodes and shows significance of each anomaly within the model.

across the top of the MTZ (Figure 6, cross section 5). Similar to the continuity of F1 and F2 into F3, F3 continues into F4.

There are other less prominent fast anomalies resolved in our model. One of these (F5) is located at roughly 200 km depth immediately to the east of F2 (Figures 5a, 5b, and 6, cross sections 4 and 5). F5 is a small anomaly that appears to be isolated from the other fast anomalies, and it has a less well-constrained geometry due to its small size. Similarly, F6 (Figures 5a, 5b, and 6, cross sections 3) is a small anomaly located in the southeastern part of the model. This is also an isolated anomaly roughly between 60 and 150 km depths, and it is enveloped in slow-velocity perturbation patterns. The surface projection of this anomaly roughly coincides with the location of the BMA and the proposed location of the SWS.

Our model reveals two prominent slow-velocity regions, S1 and S2 (Figures 5a–5d). Anomaly S1 is the largest anomaly of our resultant model, covering most of the southern half of the model space across all resolved depths in our model. We describe this anomaly’s regional variations by dividing it into western (wS1), south-central (cS1) and eastern (eS1) anomalies.

Anomaly wS1 is a smaller anomaly located beneath the northern part of the Mississippi embayment in western Tennessee and within the outline of the RFR. At its northernmost part beneath NW Tennessee, the anomaly is shallow and located above 100 km depth where it is underlain by F1 (Figure 6, cross section 5). The southern part of the anomaly below SW Tennessee extends down to 200 km depth and connects with the thicker slow-velocity anomalies below the Gulf of Mexico (Figure 6, cross sections 1 and 6).

Anomaly cS1 is located beneath the coastal plains of the Gulf of Mexico. Compared to wS1 it extends deeper into the upper mantle, reaching a maximum depth of 400 km (Figure 6, cross sections 1 and 3). This section of S1 includes some of the lowest velocities observed in our study area. Anomaly eS1 is located beneath Atlantic coastal plains and northwestern parts of Georgia and South Carolina (Figures 5a and 5b). It appears to be the northern continuation of cS1, wrapping around the southern limits of F1 and F2 and enveloping F6. Similar to cS1, it extends down to 350 to 400 km from the top of the model at its deepest parts (Figure 6, cross sections 3 and 6).

The second prominent slow-velocity anomaly is S2 (Figures 5a, 5b, and 6, cross sections 3 and 4). This anomaly is isolated from S1. It is located beneath the northern Blue Ridge Mountains of West Virginia and Virginia, where evidence of Cenozoic volcanism has been found, extending east to the coast at its northernmost extent. Anomaly S2 covers significantly smaller portion of the model compared to S1 (Table 1). It is located to the east of F1 and partially overlies F5. S2 extends from top of the model down to ~200 km depth.

5. Resolution and Recovery Tests

In an attempt to assess the robustness of the prominent features discussed above, we carry out a series of checkerboard and recovery tests. These tests help us determine the resolving power of our data set and

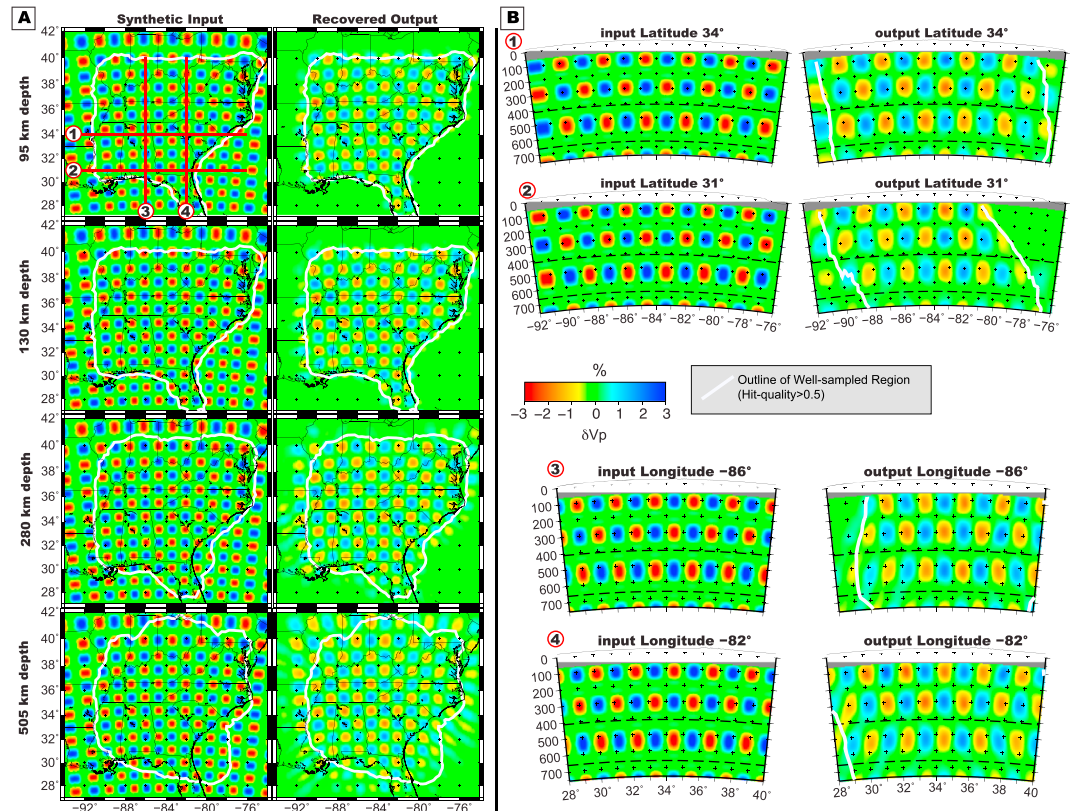


Figure 7. Results of checkerboard tests. (a) Map slices of tests results at various depths. (b) Latitudinal and longitudinal sections showing results of checkerboard tests.

reveal probable artifacts of the tomographic inversion that may exist in regions of our model that have limited or uneven sampling.

We perform checkerboard tests to investigate the vertical and lateral resolution of our inversion. These tests are ideal for identifying artifacts such as smearing and streaking along the theoretical raypaths. The checkerboard pattern that we utilize consists of multiple layers of alternating synthetic fast (+3%) and slow (−3%) velocity perturbations embedded in a neutral background (Figure 7). The results indicate that the resolution of the model is good in the central parts of the modeled volume beneath the footprint of the station array (Figure 7a, inside white outlines). The resolution decays gradually toward the periphery of the study area where the quality of sampling decreases rapidly (Figure 7b). Note that the amplitudes of the recovered anomalies are weaker compared to the original checkerboard pattern. In these tests, the peak amplitude recovery is 84% of the input anomaly and the average amplitude recovery at the center parts of the model is roughly 55%. The clearly visible amplitude loss is partly due to the minimum length solution of the inversion algorithm and is very common among similar tomographic studies. In addition, damping and smoothing constraints may also contribute to such amplitude decay and minor changes in the overall shapes of the recovered anomalies. Although the amplitudes of the recovered anomalies are affected along with small variations in the geometry of the resolved shapes, the recovery of the overall pattern is successful owing to good station coverage and dense sampling of the modeled domain. The calculated means of the recovered slow- and fast-velocity anomalies are −1.9% and +1.8%, respectively, showing that we can recover over 60% of the amplitude of the synthetic structure. It is possible to quantify the average spatial resolution scale of the model space via these checkerboard tests. The average resolution length is roughly equal to the half-length of the minimum well-recovered checkerboard anomaly dimension [Lebedev and Nolet, 2003]. Using this proxy, the lateral resolution in the central part of the upper layer of our model is roughly 40 km, and the lateral resolution gradually increases with depth up to 60 km toward the bottom of our model. The vertical resolution is roughly 50 km at the top of our model and gradually increases and exceeds 65 km toward the bottom. This reduction in resolution with depth is a direct consequence of increasing vertical spacing of nodes

(Figure 3b) and reduction in hit qualities (Figure 4) at depth. The results of these tests show that our data set and inversion algorithm are capable of resolving major lithospheric and sublithospheric structures in the parameterized volume, with a reasonable level of detail. These resolution tests caution us against over interpretation of the anomalies resolved in regions with poor sampling.

In addition to the checkerboard tests, we also carry out recovery tests using synthetic anomalies that resemble structures resolved in our model. These tests help us assess the robustness of the recovered anomalies resulting from the actual tomographic inversion. Similar to the checkerboard test, the parameters for the inversion as well as the model parameterization are kept the same as in the actual inversion. We used perturbation patterns having amplitudes of +1%, +3%, and -3% for fast and slow synthetic anomalies (Figure 8). We incorporate synthetic anomalies resembling anomalies F1–F6 (+3%) and S1–S2 (-3%) into these recovery tests. In addition, we tested recovery of the weaker amplitudes using a rectangular synthetic fast anomaly (+1%) beneath eastern North Carolina (magenta box labeled with letter X in Figure 8). We also carried out similar recovery tests for each anomaly individually, which better quantify the trade-offs between various parameters (see Figure S4 in the supporting information).

The results of these tests show that general outline of the major synthetic anomalies is recovered reasonably well. The recovery tests show minor deviations from the outlines and recovered perturbation amplitudes of the actual anomalies. These artifacts are outlined in Figure 8 with letters A and B. Similar to checkerboard tests, the recovered anomalies also have smaller perturbations than the actual synthetic anomaly. Artifact A shows the effect of the minimum length solution and consequent loss of amplitude. This can potentially result in the poor recovery of weaker and smaller perturbation patterns (Figure 8, A on cross section 2). Such weaker amplitude recovery is found over most parts of the model space but becomes more recognizable toward the periphery of the well-resolved portions of the model (Figure 8, cross section 1). These tests show that even the smaller anomalies such as F5 and F6 can be recovered in their correct positions but with some reasonable uncertainty in their exact shape and depth (Figure 8, cross section 2).

Artifact B shows the effects of vertical smearing at shallow depths within the model. Such streaking can affect the recovered dimensions of the anomalies, resulting in anomalies that extend deeper into the model than the actual anomaly (Figure 8, cross sections 2 and 3). Based on the results of these tests, the thickness and depth extent of shallow anomalies, such as F1, F2, F5, and F6 as well as shallow sections of S1 and S2 can be affected (Figure 8, cross sections 2 and 3). However, the streaked portions are associated with much smaller perturbation amplitudes. This is why the actual outlines of the input anomalies are still visible in the results of the tests (i.e., B in Figure 8, cross section 3). The general outlines and amplitudes of deeper anomalies such as F3 and F4 are resolved successfully without significant variations in dimensions. This is also true for deeper sections (below 100 km) of cS1 and eS1. Overall, minor streaking exists in our model with negligible lateral deviations in recovered anomalies. Lateral deviations are primarily due to the smoothing constraint used in the inversion.

In general, these tests caution us against the interpretation of smaller anomalies with lower perturbation magnitudes. Such a region may exist in the eastern section of our model beneath North Carolina (magenta boxes labeled with letter X in Figure 8). Our models show relatively small amplitude, shallow, fast to neutral velocity perturbations here. The results of our tests show that the +1% fast anomaly beneath North Carolina can be resolved but very weakly with poor recovery of the general shape (Figure 8, maps of 60 and 165 km depth and cross section 1). This indicates that the recovery of smaller velocity perturbations is not as good as the recovery of anomalies with greater velocity perturbations (as expected). Overall, the tests show larger-magnitude perturbations with significantly large dimensions can robustly be resolved in the model. Therefore, the imaged attributes of the anomalies F1–F4 and S1 and S2 are reliable. These tests also show that the locations of anomalies F5 and F6 are also robust but with less well-constrained geometry and depth.

6. Discussion

Our tomographic model reveals large-scale velocity heterogeneities throughout the upper mantle beneath the SEUS. Our images indicate that structural complexity in the region is likely associated with both inherited structures and structures that are currently active due to the state of the upper mantle.

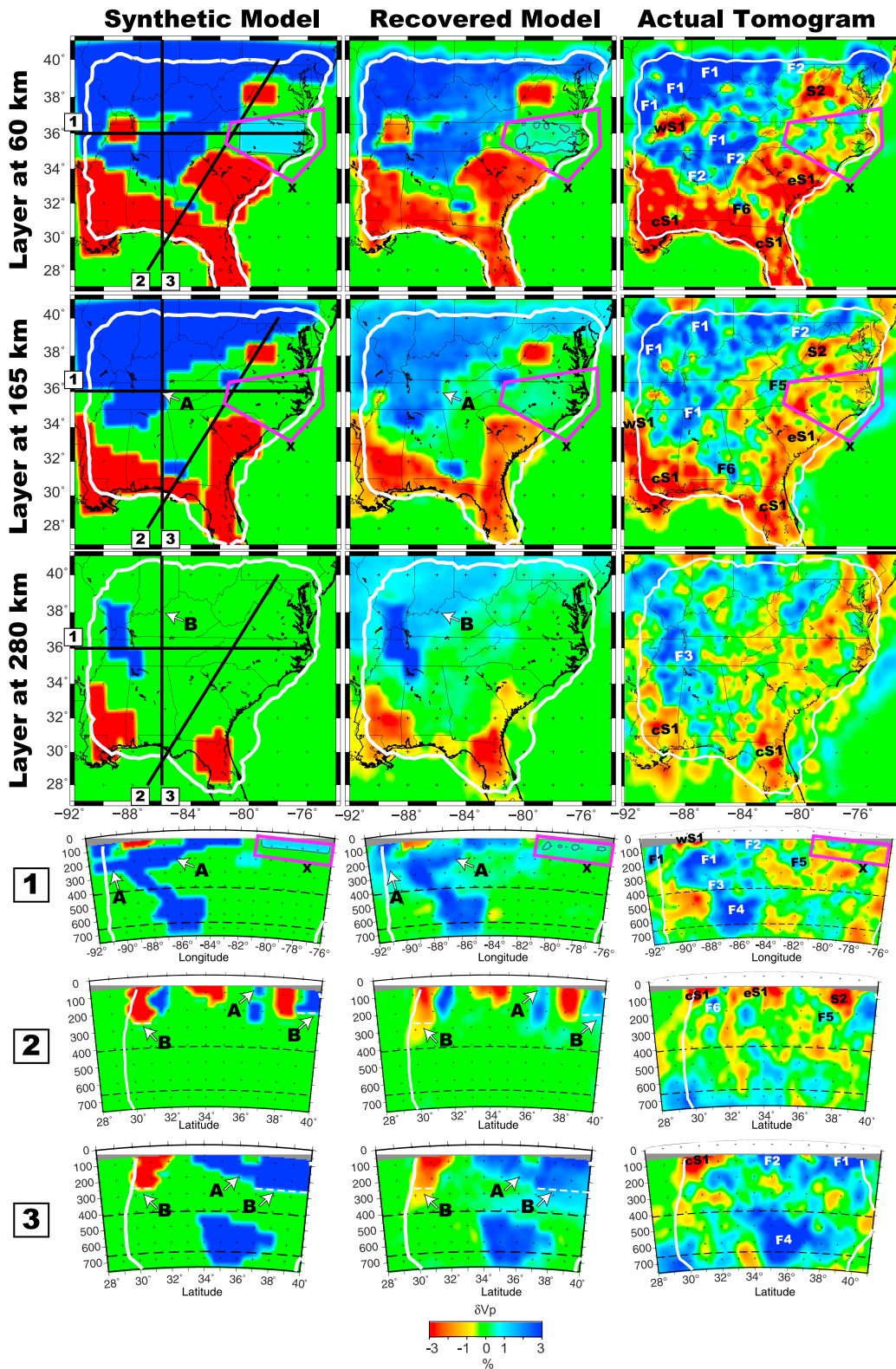


Figure 8. Results of synthetic recovery tests along with the actual tomograms of the same depth slice and same profile. Patterns A and B show minor inversion artifacts due to amplitude loss and streaking, respectively. Dashed white lines mark the expected (input) outlines of anomalies for reference. The magenta box labeled with letter X contains a lower amplitude (+1%) fast anomaly and shows recovery of smaller velocity perturbations in our model. The input and recovered anomalies are outlined with +0.5% contour in this box for emphasizing loss in recovery of the overall shape but recovery of the correct position. Locations of the profiles are also shown on the maps together with the corresponding number.

6.1. Evidence of Inherited Structures

The structures resolved in our tomographic model indicate strong correlations with the existing tectonic and geological fabric of the region. The sharp transition from the thick F1 anomaly to the thinner F2 anomaly closely follows the projection of the GF in the uppermost mantle, marking the eastern edge of the Proterozoic age Stable North American (SNA) lithosphere [Hoffman, 1988; Rychert *et al.*, 2007; French *et al.*, 2009; Abt *et al.*, 2010; Yuan and Romanowicz, 2010; Schaeffer and Lebedev, 2014; Yuan *et al.*, 2014] (Figure 9, cross sections 1–3). This transition closely follows the New York-Alabama Magnetic Lineament (NY-AL ML) [Vlahovic *et al.*, 1998; Powell *et al.*, 2014; Powell and Thomas, 2016]. However, previous studies have suggested that Grenville basement rocks likely extend significantly east of the surface expression of the Grenville margin [e.g., Cook and Vasudevan, 2006; Hibbard *et al.*, 2012]. If Grenville basement rocks do extend farther to the east, our results indicate that the underlying mantle lithosphere has been significantly modified. We discuss a plausible mechanism for such a modification in section 6.3.

Farther to the west, the slow-velocity anomaly wS1 is strongly correlated with the outline of the Mississippi embayment and the RFR. This suggests that this long-lived, inherited lapetan rifting structure has a clear mantle expression (Figure 9, cross sections 1–3). Similar observations come from the tomographic images of Pollitz and Mooney [2014], Yuan *et al.* [2014], and Schaeffer and Lebedev [2014] showing significantly slower upper mantle beneath the RFR. In addition, there is a clear spatial correlation between the outline of NMSZ and the slow-velocity anomaly wS1 (Figure 9, cross sections 1 and 2). This correlation has already been interpreted by Pollitz and Mooney [2014] as the weak, thin lithosphere of RFR emerging as a seismogenic zone. In our models, the NMSZ is located closer to the western edge of the RFR. Therefore, our results may indicate that the NMSZ reflects stress concentration along a sharp zone of lithospheric thickness change beneath the flanks of the rift, similar to the mechanism proposed by Zhang *et al.* [2009] based on Pn tomography results from the SEUS.

Anomaly F6 underlies and roughly parallels the E-W trend of the BMA (see map in Figure 9) and inferred Suwannee suture [Mueller *et al.*, 2014]. The limited extent and resolution of this anomaly renders it difficult to link to either Laurentian or Gondwanan lithosphere. However, if F6 is of lithospheric affinity, it may be a remnant lithospheric fragment within the collision zone.

6.2. Links Between Observed Structures and Ongoing Tectonism

The patterns and structures resolved in our tomographic model also show clear correlations with active tectonism and dynamic attributes of this region. The Cenozoic volcanic centers of western Virginia (48 Ma [Mazza *et al.*, 2014]) are underlain by S2, which in turn is underlain, in part, by F5 (Figure 9, cross section 1). There are various studies that report slow velocities beneath central Virginia similar to our S2 anomaly [Chu *et al.*, 2013; Schmandt and Lin, 2014; Liu and Holt, 2015]. The recovery and resolution tests show that the outline and position of S2 can be reliably resolved (Figures 7 and 8). One possible interpretation of these anomalies is that F5 is a portion of mantle lithosphere that has delaminated, and S2 is the asthenosphere that filled the void (Figure 9, cross section 1). Support for this delamination hypothesis comes from the presence of the GCSZ and CVSZ that lie at the periphery of the shallowest resolved portions of S2 (Figure 9, map and cross section 1). This may indicate a change in lithospheric thickness and, hence, strength. Mazza *et al.* [2014] proposed delamination as the driving mechanism of volcanism for this region based on the geochemical attributes of the exposed volcanic suite. Here we present seismic evidence that such a delamination likely did occur in a piecemeal fashion and that one of the more recently removed lithospheric fragments (F5) may still be visible. Similar observations of removed mantle lithosphere and intraplate volcanism can be found along the RFR, where cS1 underlies volcanic centers located near the coast (V2 and V3, Figure 1). Even though these centers are buried beneath the thick sedimentary cover of the Mississippi embayment, the existence of high heat flow observations [Smith and Dees, 1982; Ruppel *et al.*, 2005] strongly suggests the presence of young intraplate volcanism [Braunstein and McMichael, 1976; Vogt and Jung, 2007].

Another active deformation zone within our study area is the ETSZ. This zone is located near the GF at the eastern edge of stable North America (Figure 9, map and cross sections 2 and 3). The sharp lithospheric thickness variation beneath this zone from F1 to F2 may result in stress localization that could be in part responsible for the observed seismicity [Vlahovic *et al.*, 1998; Zhang *et al.*, 2009; Powell *et al.*, 2014;

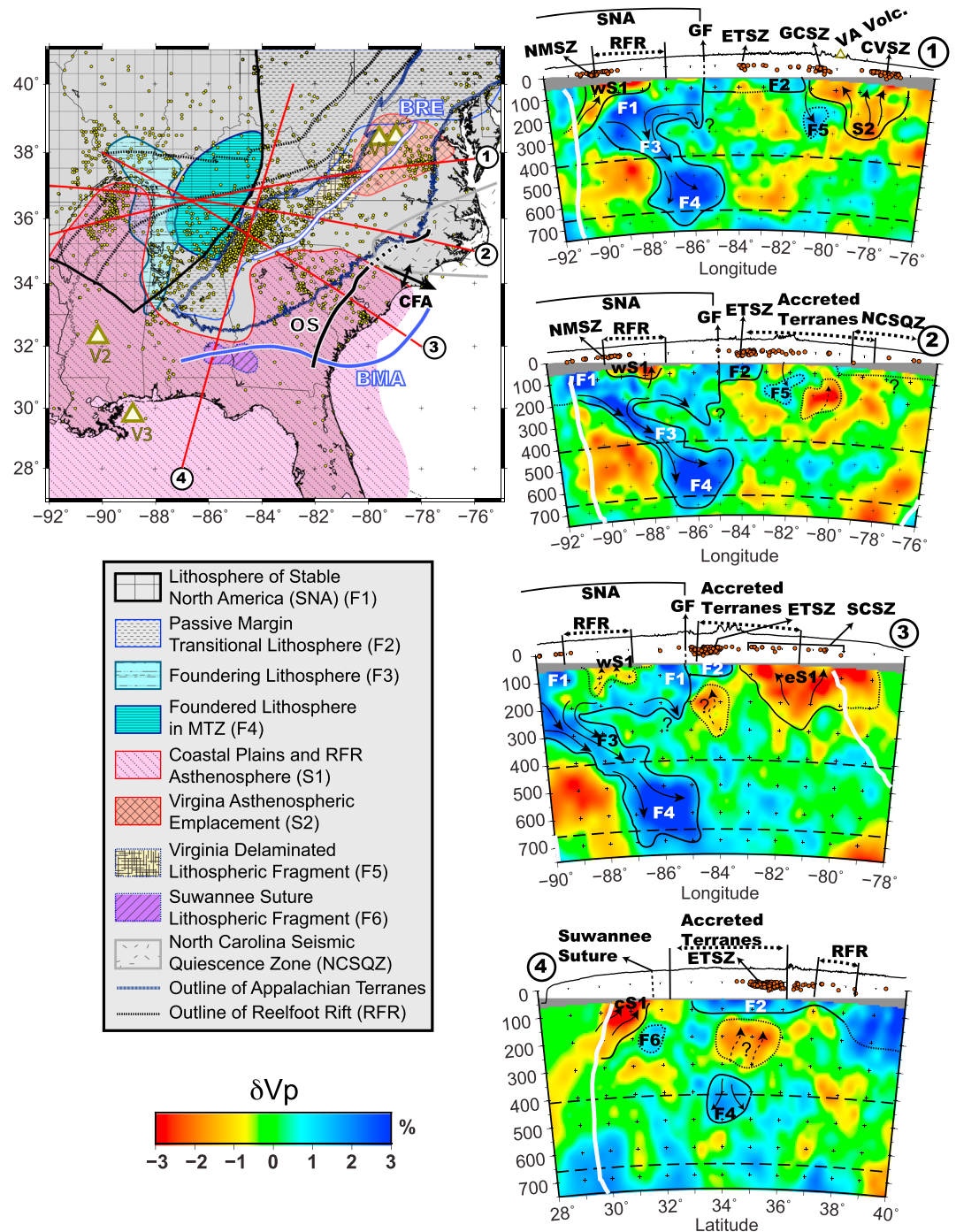


Figure 9. Results of the analysis together with the interpretations of the resolved anomalies. All interpreted structures are outlined and labeled accordingly. Black arrows on these indicate the direction of removal (F1–F5) and asthenospheric emplacement (S1–S2). Major crustal structures and terranes are labeled along the topographic profile of each cross section (vertical exaggeration: x15). The reference map shows the general outlines of all the interpreted features (F1–F6 and S1–S2). Major Volcanic centers (V1–V3) and lithospheric structures are labeled on the map. BRE = Blue Ridge Escarpment; CFA = Cape Fear Arch, OS = Orangeburg Scarp. ETSZ = Eastern Tennessee Seismic Zone, NMSZ = New Madrid Seismic Zone, GCSZ = Giles County Seismic Zone, SCSZ = South Carolina Seismic Zone, CVSZ = Central Virginia Seismic Zone. Seismicity is from the Virginia Tech Seismological Observatory catalog (1900–2014).

Powell and Thomas, 2016]. Such localization provides the driving mechanism for the reactivation of the mid-crustal structures within the crystalline basement rocks.

Along the coastal plains, a clear spatial association exists between seismogenic zones and the outline of eS1. The seismically quiet zone in North Carolina (see map in Figure 9) and southernmost Virginia is bounded by eS1 to the south and by S2 to the north. Seismic velocities in between eS1 and S2 within the zone of seismic quiescence are significantly less slow than surrounding areas, which may indicate stronger mantle lithosphere in this area (Figure 9, cross section 2 versus cross sections 1 and 3). In addition to the along-strike variability in seismicity, there are other intriguing observations of ongoing tectonism that coincide with the along-strike variation in uppermost mantle velocities. For example, the CFA is located above the transition between eS1 and the faster uppermost mantle speeds beneath North Carolina. This also coincides with the peak elevation of the OS, possibly indicating a correlation between mantle velocity perturbations and crustal deformation (Figure 9, map). Farther to the west, the BRE roughly marks the transition from faster uppermost mantle speeds in the west associated with thicker lithosphere (F1 and F2) to the slower uppermost mantle of the coastal plains (Figure 9, map and cross section 3). The Pn velocities in MacDougall *et al.* [2015] sample the transition from F2 to eS1 just below the Moho. Interestingly, the reported Pn velocities are low beneath the BRE and higher farther southeast, opposite of what our model shows. This discrepancy could be due to the detection of a vertically localized, thinner layer by Pn phases that could not be resolved in our study. The change of upper mantle velocities beneath the BRE in our model is similar to the variations that we observe beneath the CFA and the peak of the OS and suggests that the upper mantle might play a role in their evolution [Winker and Howard, 1977; Bartholomew and Rich, 2013; Rowley *et al.*, 2013]. However, the exact mechanism for such tectonism and deformation requires further geodynamic investigation.

6.3. Deeper Structure and Evolution

One of the most prominent features in our inversion is the large eastward dipping fast anomaly F3 that connects to the smaller but faster anomaly F4 in the transition zone. There are an increasing number of studies that report fast structures in the uppermost mantle with irregular geometries beneath the SEUS, similar to our F3 and F4 anomalies [Wagner *et al.*, 2012; Chu *et al.*, 2013; Evanzia *et al.*, 2014; Yuan *et al.*, 2014; Schmandt and Lin, 2014]. Particularly, the location of F4 in the mantle transition zone agrees quite well with the fast anomalies resolved in the tomographic model of Schmandt and Lin [2014]. Our model provides a more detailed image of this structure beneath SEUS, revealing its relationship to other mantle and lithospheric features. Here we evaluate possible interpretations for this dipping, sublithospheric structure and delineate major strengths and weaknesses of each interpretation.

Dipping high-velocity anomalies in the upper mantle that extend to depths of 200 km or greater are often interpreted as subducting or subducted oceanic lithosphere [e.g., Biryol *et al.*, 2011; Schmandt and Humphreys, 2011; Porritt *et al.*, 2014]. We explore two possible subduction-related explanations for our F3/F4 anomalies (a Grenville-age relict slab or part of the inboard extent of the Farallon flat slab) before presenting an alternative and preferred model (lithospheric removal related to Rayleigh-Taylor instability).

The strongest argument in favor of our F3/F4 anomaly being a relict, 1 Ga Grenville slab fragment is that the shallowest portions of our observed anomaly coincide with the location of the deformation front of the Grenville Orogeny. In order for this to be a Grenville age slab, the current GF would have to match the ancient convergent plate boundary and the slab would have had to stay attached, despite its initial negative buoyancy. The exact location and geometry of the plate margin as well as the subduction polarity at that time is obscured by subsequent episodes of rifting, accretion, and orogeny during the following Wilson cycle [Thomas, 2006]. A direct attachment to the overriding lithosphere would help to explain how the slab avoided sinking into the lower mantle over such a prolonged time period, but how it remained attached when many other, younger slabs have failed to do so is unclear. While Proterozoic fossil slabs of similar dimensions and geometries have been imaged and interpreted beneath different parts of North America in previous studies [Yuan and Dueker, 2005; Porritt *et al.*, 2014], there is no clear consensus about the mechanism that would explain stagnation and neutral buoyancy of these slabs. Proposed mechanisms generally involve limiting subducted slab density by thermally impeded eclogitization of the crustal component and its eventual removal via melting [Bjornerud and Austrheim, 2004; Yuan and Dueker, 2005; Schmandt and Humphreys, 2011].

The fast anomaly resolved in our tomograms could also be the leading edge of the flat Farallon slab (~80 Ma) that stagnated in the upper mantle following a detachment phase that took place between 50 and 20 Ma [Humphreys, 1995]. The easterly position of the anomaly with respect to the western North America plate margin could be attributed to the well-accepted initial, broad flat-slab geometry, together with the subsequent westward relative motion of the North America plate over the slab fragment following its detachment. This interpretation also has similar drawbacks to the Grenville slab interpretation. First and foremost, a mechanism is required to transform the slab into a neutrally buoyant state to explain its stagnation in the upper mantle. In this case, unlike the Grenville slab, the Farallon slab is not attached to the overriding lithosphere, so there is no factor other than neutral buoyancy to prevent it from sinking. The relatively shallow depth of F3 indicates that it experienced little sinking and maintained its outline and integrity while passing below the 150–200 km thick lithosphere of the stable interior of North America [Yuan and Romanowicz, 2010]. We have performed additional recovery tests to show that our model is capable of revealing a gap between F1 and F3 if it is greater than 100 km (see Figure S5 in the supporting information). The fact that we do not observe such a gap in our model indicates that if this feature were the Farallon slab, it would have descended less than 100 km since its subduction 80 Myr ago. It is also worth noting that another fast-velocity pattern has already been interpreted as the remnants of the Farallon slab at much greater depths than F3 and F4 in the lower mantle beneath the SEUS [Grand, 1994; Van der Hilst et al., 1997; Ritsema et al., 1999; Mégnin and Romanowicz, 2000; Sigloch, 2011; Burdick et al., 2014; Porritt et al., 2014; Schmandt and Lin, 2014].

We propose an alternative explanation for our fast *P* wave anomalies that does not invoke subduction at all. It is possible that our F3/F4 anomalies reflect dense lithospheric mantle that has been partially removed due to Rayleigh-Taylor instability. In general, this foundering can happen either as a wholesale peeling away of mantle lithosphere (“delamination”), or a partial, more viscous removal of lithosphere (“drip”) [Gogus and Pysklywec, 2008]. Lithospheric drips are generally much faster, more localized, and appear as steeply dipping cylindrical fast anomalies in the upper mantle [i.e., West et al., 2009; Van Wijk et al., 2010]. Both delamination and drips may be associated with magmatic activity. The factors that control the initiation of foundering are not well understood, but recent studies suggest a mechanical/thermal destabilization of dense eclogitic or ultramafic roots of continental lithosphere due to external factors such as plutonism or convective instability at cratonic edges [Zandt et al., 2004; West et al., 2009; Kaislaniemi and van Hunen, 2014]. We know of no example of ongoing lithospheric foundering that is as regionally extensive as the high-velocity anomalies we observe. However, in contrast to subduction-related explanations, ongoing, possibly sporadic foundering of portions of the lithosphere beneath the SEUS could help to explain a number of the tectonic observations discussed above. For example, the removal of lithospheric mantle from the bottom of the plate could help to explain the thinner lithosphere of regions east of F2. Given that previous work has suggested that Grenville basement crust extends eastward to the coastal plain, the variation in lithospheric thickness between F1 and F2 either implies a coincidental spatial agreement between the GF and the F1/F2 thickness variation or may imply that the GF separates zones of lithosphere with different styles of foundering and degree of removal. Because the GF is roughly the western limit of the later Appalachian orogen in the SEUS [Thomas, 2006], the reworked nature of the lithosphere to its east may have been more susceptible to instability following multiple episodes of subduction and lithospheric shortening. This sort of piecemeal delamination beneath large orogens is a well-documented occurrence [Beck et al., 2014].

Piecemeal or regional lithospheric removal could also lead to the replacement of removed lithospheric pieces with hot and more buoyant asthenospheric inflow. The resultant partial melting could help to explain observed postorogenic intraplate volcanism (Figure 9). Such lithospheric removal also helps explain the lack of consistency in the spatial and temporal distributions of seismogenic zones. Delamination could result in broad areas of weaker lithosphere, and zones of abrupt lithospheric thickness variations might act as stress concentrators [Zhang et al., 2009; Pollitz and Mooney, 2014]. The clearest evidence for this in the study area is the locations of the NMSZ and the ETSZ at sharp transitions in lithospheric thickness and along the eastern and western margins of the stable interior (F1). Similarly, higher seismic velocities beneath North Carolina may be due to stronger, better-preserved lithosphere and hence lack of seismicity in such regions (see NCSQZ in Figure 9, map and cross section 2). The regions of relatively thinner lithosphere are underlain by hot asthenosphere, making them thermally weaker, leading to broad regions of increased seismicity. The

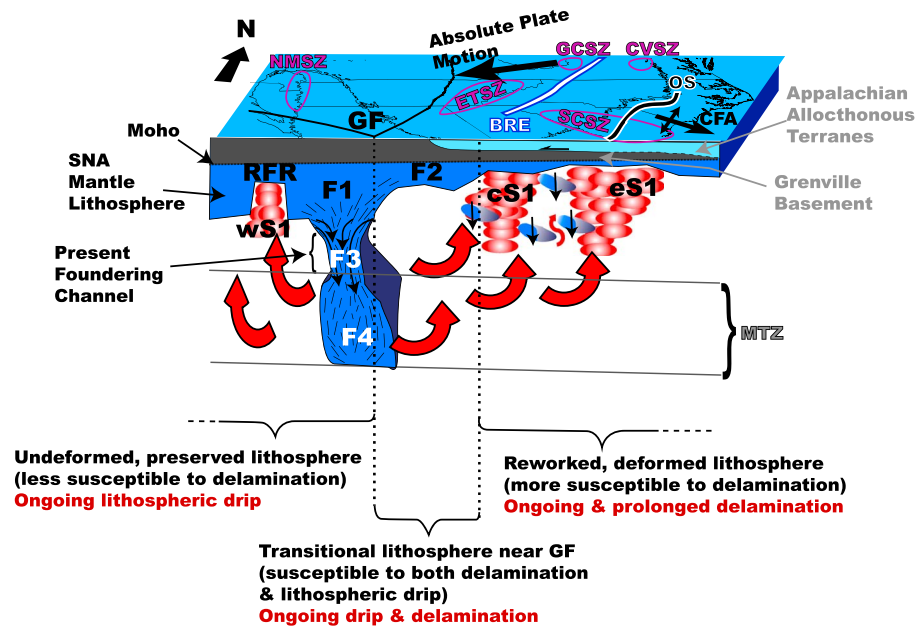


Figure 10. A conceptual model of the upper mantle structure beneath the study area based on seismic images and various observations of tectonism in the region (see Figure 9 for abbreviations). Interpreted visible anomalies (F1–F5, S1) are also labeled in the figure. Variations in lithospheric removal styles and inferred nature of the lithosphere of each section of the model are summarized at the bottom. The black arrows on lithospheric fragments and the dripping part indicate sense of removal and foundering. Note the dip of F3/F4 is in agreement with the motion of the overriding North American lithosphere with respect to the asthenosphere below. Black arrow at top shows absolute plate motion direction (HS3-NUVEL-1A [Gripp and Gordon, 2002]). Red arrows show asthenospheric return flow.

best example for such a zone is the SCSZ, which is completely underlain by eS1 (Figure 9). Similar relationships also exist for the CVSZ, which is partially underlain by S2. In addition to volcanism and seismicity, large zones of slow upper mantle and spatial variations between thicker/stronger lithosphere and thinner/weaker lithosphere might help to explain upwarping of coastal plains as well as distinct geomorphic features such as the BRE due to epeirogeny and differential deformation.

It is not possible to know how much mantle lithosphere previously existed beneath the SEUS prior to this proposed delamination/drip. It is also not possible to know exactly when and how fast lithospheric mantle was removed. However, based on the current configuration revealed in our tomographic model, we can infer a general time and spatial framework for lithospheric removal. Given the young intraplate volcanism and ongoing tectonism in the region east of the GF, we propose that the piecemeal removal in the form of delamination was active throughout the Cenozoic. It is also possible that the deformation of lithosphere to the east of the GF during repeated episodes of subduction and rifting resulted in the onset of lithospheric removal much earlier than the Cenozoic. The shallow location of lithospheric fragments such as F5 east of the GF suggests that this removal may still be ongoing.

The general shape of the F3/F4 anomalies suggests that the style of removal is more drip-like than delamination, perhaps due to the change in mechanical characteristics of the lithosphere from the more heavily deformed F2 to better preserved F1 (Figure 10). The large volume of F4 may have been slowly and continuously accumulating, as foundering lithosphere (F3) progressed and stalled in the MTZ (Figure 10). A slow rate of removal can also explain slow strain rates experienced in major seismogenic zones of the region (NMSZ and ETSZ) [Powell et al., 1994; Newman et al., 1999]. This drip-like foundering event can also pose as a plausible driving mechanism for return flow of asthenosphere along the RFR as well as eastern S1 beneath the Gulf of Mexico and Atlantic Coastal Plains (Figures 9 and 10). In addition, the eastward dip direction of the present foundering lithosphere (F3) is roughly in agreement with WSW directed absolute plate motion of the North American Plate [Gripp and Gordon, 2002]. If such foundering is taking place beneath the SEUS as a continuous process, then the portions that foundered earlier would be located farther east (Figure 10).

7. Conclusions

Our tomographic images provide a well-resolved snapshot of the upper mantle beneath the SEUS. Based on these images, the SEUS has a much more complicated upper mantle than previously thought. Our model indicates a heterogeneous upper mantle with significant lithospheric variations. The images clearly reveal the edge of the stable interior of the North America Plate along the surface expression of the Grenville front and western margins of the Appalachian orogeny. These structures, along with the RFR, appear to be important inherited features that affect localized tectonism. However, tectonic inheritance does not explain all of the ongoing tectonism experienced in the region. Our models show a well-resolved, seismically fast, eastward dipping structure that we propose to represent foundering of lithospheric mantle. This process could help to explain the variable tectonism observed across our study area. Our results suggest that tectonic inheritance is important, but ongoing dynamic and magmatic processes are also required to explain mantle structure and tectonic activity in the passive margin lithosphere.

Acknowledgments

We would like to thank members of the field crew for their help and efforts during deployment and service of the SESAME array; Kevin G. Stewart, Lijun Liu, and Sarah Mazza for useful discussions. The seismic equipment for this project was provided by the EarthScope program through the IRIS-PASSCAL consortium. The seismic data will be available through the IRIS Data Management Center. This work was funded by the NSF EarthScope Program under the American Recovery and Reinvestment Act of 2009 (Public Law 111-5) through awards EAR-0844186, EAR-0844276, and EAR-0844154.

References

- Abt, D. L., K. M. Fischer, S. W. French, H. A. Ford, H. Y. Yuan, and B. Romanowicz (2010), North American lithospheric discontinuity structure imaged by Ps and Sp receiver functions, *J. Geophys. Res.*, *115*, B09301, doi:10.1029/2009JB006914.
- Albuquerque Seismological Laboratory (ASL)/USGS (1988), Global Seismograph Network (GSN - IRIS/USGS), Int. Fed. of Digital Seismograph Networks, doi:10.7914/SN/IU.
- Bartholomew, M. J., and F. J. Rich (2013), Pleistocene shorelines and coastal rivers: Sensitive potential indicators of Quaternary tectonism along the Atlantic coastal plain of North America, *Geol. Soc. Am. Spec. Pap.*, *493*, 17–36.
- Bartholomew, M. J., B. M. Brodie, R. H. Willoughby, S. E. Lewis, and F. H. Syms (2002), Mid-Tertiary paleoseismites: Syndepositional features and section restoration used to indicate paleoseismicity, Atlantic Coastal Plain, South Carolina and Georgia, *Geol. Soc. Am. Spec. Pap.*, *359*, 63–74.
- Beck, S. L., G. Zandt, K. M. Ward, and A. Scire (2014), Multiple styles and scales of lithospheric foundering beneath the Puna Plateau, central Andes, *Geol. Soc. Am. Mem.*, *212*, 43–60.
- Biryol, C. B., S. L. Beck, G. Zandt, and A. A. Özacar (2011), Segmented African lithosphere beneath the Anatolian region inferred from teleseismic P-wave tomography, *Geophys. J. Int.*, *184*, 1037–1057.
- Bjornerud, M. G., and H. Austrheim (2004), Inhibited eclogite formation: The key to the rapid growth of strong and buoyant Archean continental crust, *Geology*, *32*, 765–768.
- Blackburn, T. J., P. E. Olsen, S. A. Bowring, N. M. McLean, D. V. Kent, J. Puffer, G. McHone, E. T. Rasbury, and M. Et-Touhami (2013), Zircon U-Pb geochronology links the end-Triassic extinction with the Central Atlantic magmatic province, *Science*, *340*, 941–945.
- Bollinger, G., and R. L. Wheeler (1983), The Giles County, Virginia, seismic zone, *Science*, *219*, 1063–1065.
- Braunstein, J., and C. McMichael (1976), Door Point: A buried volcano in southeast Louisiana, *Gulf Coast Assoc. Geol. Soc. Trans.*, *26*, 79–80.
- Burdick, S., R. D. Van der Hilst, F. L. Vernon, V. Martynov, T. Cox, J. Eakins, G. H. Karasu, J. Tylell, L. Astiz, and G. L. Pavlis (2014), Model update January 2013: Upper mantle heterogeneity beneath North America from travel-time tomography with global and USArray transportable array data, *Seismol. Res. Lett.*, *85*, 77–81.
- Burke, K., and J. Dewey (1973), Plume-generated triple junctions: Key indicators in applying plate tectonics to old rocks, *J. Geol.*, *81*, 406–433.
- Chiu, J. M. (2010), Exploring seismic velocity of sediments in the Mississippi embayment, Int. Fed. of Digital Seismograph Networks, doi:10.7914/SN/3E_2010.
- Chu, R., W. Leng, D. V. Helmberger, and M. Gurnis (2013), Hidden hotspot track beneath the eastern United States, *Nat. Geosci.*, *6*, 963–966.
- Cook, F. A., and K. Vasudevan (2006), Reprocessing and enhanced interpretation of the initial COCORP Southern Appalachians traverse, *Tectonophysics*, *420*, 161–174.
- Cook, F. A., D. S. Albaugh, L. D. Brown, S. Kaufman, J. E. Oliver, and R. D. Hatcher (1979), Thin-skinned tectonics in the crystalline southern Appalachians: COCORP seismic-reflection profiling of the Blue Ridge and Piedmont, *Geology*, *7*, 563–567.
- Culotta, R. C., T. Pratt, and J. Oliver (1990), A tale of two sutures: COCORP's deep seismic surveys of the Grenville province in the eastern U.S. midcontinent, *Geology*, *18*, 646–649.
- Dahlen, F., S.-H. Hung, and G. Nolet (2000), Fréchet kernels for finite-frequency traveltimes—I. Theory, *Geophys. J. Int.*, *141*, 157–174.
- Denison, R. E., M. Bickford, E. G. Lidiak, and E. B. Kisvarsanyi (1987), Geology and geochronology of Precambrian rocks in the central interior region of the United States.
- Ervin, C. P., and L. McGinnis (1975), Reelfoot rift: Reactivated precursor to the Mississippi embayment, *Geol. Soc. Am. Bull.*, *86*, 1287–1295.
- Evanzia, D., J. Pulliam, R. Ainsworth, H. Gurrula, and K. Pratt (2014), Seismic Vp & Vs tomography of Texas & Oklahoma with a focus on the Gulf Coast margin, *Earth Planet. Sci. Lett.*, *402*, 148–156.
- Fischer, K. M., R. B. Hawman, and L. S. Wagner (2010), Southeastern suture of the Appalachian margin experiment, Int. Fed. of Digital Seismograph Networks, doi:10.7914/SN/Z9_2010.
- French, S., K. Fischer, E. Syracuse, and M. Wyssession (2009), Crustal structure beneath the Florida-to-Edmonton broadband seismometer array, *Geophys. Res. Lett.*, *36*, L08309, doi:10.1029/2008GL036331.
- Gallen, S. F., K. W. Wegmann, and D. R. Bohnenstiehl (2013), Miocene rejuvenation of topographic relief in the southern Appalachians, *GSA Today*, *23*, 4–10.
- Gogus, O. H., and R. N. Pysklywec (2008), Near-surface diagnostics of dripping or delaminating lithosphere, *J. Geophys. Res.*, *113*, B11404, doi:10.1029/2007JB005123.
- Grand, S. P. (1994), Mantle shear structure beneath the Americas and surrounding oceans, *J. Geophys. Res.*, *99*, 11,591–11,621, doi:10.1029/94JB00042.
- Gripp, A. E., and R. G. Gordon (2002), Young tracks of hotspots and current plate velocities, *Geophys. J. Int.*, *150*, 321–361.
- Harris, L. D., and K. C. Bayer (1979), Sequential development of the Appalachian orogen above a master decollement—A hypothesis, *Geology*, *7*, 568–572.
- Hatcher, R. D. (2010), The Appalachian orogen: A brief summary, *Geol. Soc. Am. Mem.*, *206*, 1–19.

- Hawman, R. B. (2008), Crustal thickness variations across the Blue Ridge Mountains, southern Appalachians: An alternative procedure for migrating wide-angle reflection data, *Bull. Seismol. Soc. Am.*, *98*, 469–475.
- Hawman, R. B., M. O. Khalifa, and M. S. Baker (2012), Isostatic compensation for a portion of the Southern Appalachians: Evidence from a reconnaissance study using wide-angle, three-component seismic soundings, *Geol. Soc. Am. Bull.*, *124*, 291–317.
- Hersey, J. B., E. Bunce, R. F. Wyrick, and F. Dietz (1959), Geophysical investigation of the continental margin between Cape Henry, Virginia, and Jacksonville, Florida, *Geol. Soc. Am. Bull.*, *70*, 437–466.
- Hibbard, J. (2000), Docking Carolina: Mid-Paleozoic accretion in the southern Appalachians, *Geology*, *28*, 127–130.
- Hibbard, J. P., B. V. Miller, W. E. Hames, I. D. Standard, J. S. Allen, S. B. Lavallee, and I. B. Boland (2012), Kinematics, U-Pb geochronology, and $^{40}\text{Ar}/^{39}\text{Ar}$ thermochronology of the Gold Hill shear zone, North Carolina: The Cherokee orogeny in Carolina, southern Appalachians, *Geol. Soc. Am. Bull.*, *124*, 643–656.
- Higgins, M. W., and I. Zietz (1983), Geologic interpretation of geophysical maps of the pre-Cretaceous “basement” beneath the Coastal Plain of the southeastern United States, *Geol. Soc. Am. Mem.*, *158*, 125–130.
- Hildenbrand, T. G., and J. D. Hendricks (1995), Geophysical setting of the Reelfoot rift and relations between rift structures and the New Madrid seismic zone.
- Hoffman, P. F. (1988), United Plates of America, the birth of a craton: Early Proterozoic assembly and growth of Laurentia, *Annu. Rev. Earth Planet. Sci.*, *16*, 543–603.
- Huddleston, P. F. (1993), *A Revision of the Lithostratigraphic Units of the Coastal Plain of Georgia: The Oligocene*, Ga. Geol. Surv., Atlanta, GA.
- Humphreys, E. D. (1995), Post-Laramide removal of the Farallon slab, western United States, *Geology*, *23*, 987–990.
- IRIS Transportable Array (2003), USArray transportable array, Int. Fed. of Digital Seismograph Network, doi:10.7914/SN/TA.
- Iverson, W. P., and S. B. Smithson (1983), Reprocessing and reinterpretation of COCORP Southern Appalachian profiles, *Earth Planet. Sci. Lett.*, *62*, 75–90.
- Johnston, A. C. (1996), Seismic moment assessment of earthquakes in stable continental regions—III. New Madrid 1811–1812, Charleston 1886 and Lisbon 1755, *Geophys. J. Int.*, *126*, 314–344.
- Kaislaniemi, L., and J. van Hunen (2014), Dynamics of lithospheric thinning and mantle melting by edge-driven convection: Application to Moroccan Atlas mountains, *Geochem. Geophys. Geosyst.*, *15*, 3175–3189, doi:10.1002/2014GC005414.
- Kennett, B., E. Engdahl, and R. Buland (1995), Constraints on seismic velocities in the Earth from traveltimes, *Geophys. J. Int.*, *122*, 108–124.
- Langston, C., and H. DeShon (2009), Detection and location of non-volcanic tremor in the New Madrid Seismic Zone, Int. Fed. of Digital Seismograph Networks, doi:10.7914/SN/Y8_2009.
- Lebedev, S., and G. Nolet (2003), Upper mantle beneath Southeast Asia from S velocity tomography, *J. Geophys. Res.*, *108*(B1), 2048, doi:10.1029/2000JB000073.
- Liu, L. J. (2014), Rejuvenation of Appalachian topography caused by subsidence-induced differential erosion, *Nat. Geosci.*, *7*, 518–523.
- Liu, Y., and W. E. Holt (2015), Wave gradiometry and its link with Helmholtz equation solutions applied to USArray in the eastern U.S., *J. Geophys. Res. Solid Earth*, *120*, 5717–5746, doi:10.1002/2015JB011982.
- Long, M., and P. Wiita (2013), Mid-Atlantic geophysical integrative collaboration, Int. Fed. of Digital Seismograph Networks, doi:10.7914/SN/7A_2013.
- MacDougall, J. G., K. M. Fischer, D. W. Forsyth, R. B. Hawman, and L. S. Wagner (2015), Shallow mantle velocities beneath the southern Appalachians from Pn phases, *Geophys. Res. Lett.*, *42*, 339–345, doi:10.1002/2014GL062714.
- Marple, R. T., and P. Talwani (1993), Evidence of possible tectonic upwarping along the South Carolina coastal plain from an examination of river morphology and elevation data, *Geology*, *21*, 651–654.
- Marquering, H., F. Dahlen, and G. Nolet (1999), Three-dimensional sensitivity kernels for finite-frequency traveltimes: The banana-doughnut paradox, *Geophys. J. Int.*, *137*, 805–815.
- Marzoli, A., P. R. Renne, E. M. Piccirillo, M. Ernesto, G. Bellieni, and A. De Min (1999), Extensive 200-million-year-old continental flood basalts of the Central Atlantic Magmatic Province, *Science*, *284*, 616–618.
- Mazza, S. E., E. Gazel, E. A. Johnson, M. J. Kunk, R. McAleer, J. A. Spotila, M. Bizimis, and D. S. Coleman (2014), Volcanoes of the passive margin: The youngest magmatic event in eastern North America, *Geology*, *42*, 483–486.
- Mégnin, C., and B. Romanowicz (2000), The three-dimensional shear velocity structure of the mantle from the inversion of body, surface and higher-mode waveforms, *Geophys. J. Int.*, *143*, 709–728.
- Miller, S. R., P. B. Sak, E. Kirby, and P. R. Bierman (2013), Neogene rejuvenation of central Appalachian topography: Evidence for differential rock uplift from stream profiles and erosion rates, *Earth Planet. Sci. Lett.*, *369*, 1–12.
- Moidaki, M., S. S. Gao, K. H. Liu, M. G. Abdelsalam, J. P. Hogan, and E. Atekwana (2010), Converted P-to-S phase and Moho quality beneath the New Madrid seismic zone from receiver function studies, *Geosci. Res.*, *1*(1), 7–21.
- Mueller, P. A., A. L. Heatherington, D. A. Foster, W. A. Thomas, and J. L. Wooden (2014), The Suwannee suture: Significance for Gondwana-Laurentia terrane transfer and formation of Pangaea, *Gondwana Res.*, *26*, 365–373.
- Newman, A., S. Stein, J. Weber, J. Engeln, A. Mao, and T. Dixon (1999), Slow deformation and lower seismic hazard at the New Madrid seismic zone, *Science*, *284*, 619–621.
- Nolet, G., F. A. Dahlen, and R. Montelli (2005), Traveltimes and amplitudes of seismic waves: A re-assessment, in *Seismic Earth: Array Analysis of Broadband Seismograms*, pp. 37–47, AGU, Washington, D. C.
- Paige, C. C., and M. A. Saunders (1982), LSQR—An algorithm for sparse linear-equations and sparse least-squares, *ACM Trans. Math. Software*, *8*, 43–71.
- Parker, E. H., R. B. Hawman, K. M. Fischer, and L. S. Wagner (2013), Crustal evolution across the southern Appalachians: Initial results from the SESAME broadband array, *Geophys. Res. Lett.*, *40*, 3853–3857, doi:10.1002/grl.50761.
- Parker, E. H., R. B. Hawman, K. M. Fischer, and L. S. Wagner (2015), Constraining lithologic variability along the Alleghanian detachment in the southern Appalachians using passive-source seismology, *Geology*, *43*, 431–434.
- Pavlis, G. L., and H. Gilbert (2011), Structure and dynamics of the North American Craton, Int. Fed. of Digital Seismograph Networks, doi:10.7914/SN/XO_2011.
- Pavlis, G. L., and F. L. Vernon (2010), Array processing of teleseismic body waves with the USArray, *Comput. Geosci.*, *36*, 910–920.
- Pazzaglia, F. J., and T. W. Gardner (1994), Late Cenozoic flexural deformation of the middle U.S. Atlantic passive margin, *J. Geophys. Res.*, *99*, 12,143–12,157, doi:10.1029/93JB03130.
- Pazzaglia, F. J., and T. W. Gardner (2000), *Late Cenozoic Landscape Evolution of the U.S. Atlantic Passive Margin: Insights Into a North American Great Escarpment*, Wiley, Chichester, U. K.
- Pollitz, F. F., and W. D. Mooney (2014), Seismic structure of the Central U.S. crust and shallow upper mantle: Uniqueness of the Reelfoot Rift, *Earth Planet. Sci. Lett.*, *402*, 157–166.

- Pollitz, F. F., L. Kellogg, and R. Bürgmann (2001), Sinking mafic body in a reactivated lower crust: A mechanism for stress concentration at the New Madrid seismic zone, *Bull. Seismol. Soc. Am.*, *91*(6), 1882–1897.
- Porritt, R. W., R. M. Allen, and F. F. Pollitz (2014), Seismic imaging east of the Rocky Mountains with USArray, *Earth Planet. Sci. Lett.*, *402*, 16–25.
- Powell, C. A., and W. A. Thomas (2016), Grenville basement structure associated with the Eastern Tennessee seismic zone, southeastern USA, *Geology*, *44*, 39–42, doi:10.1130/G37269.1.
- Powell, C. A., G. Bollinger, M. C. Chapman, M. S. Sibol, A. C. Johnston, and R. L. Wheeler (1994), A seismotectonic model for the 300-kilometer-long eastern Tennessee seismic zone, *Science*, *264*, 686–688.
- Powell, C. A., M. M. Withers, R. T. Cox, G. Vlahovic, and P. Arroucau (2014), Crustal velocity structure associated with the eastern Tennessee seismic zone: V_p and V_s images based upon local earthquake tomography, *J. Geophys. Res. Solid Earth*, *119*, 464–489, doi:10.1002/2013JB010433.
- Pratt, T. L., J. W. Horton, D. B. Spears, A. K. Gilmer, and D. E. McNamara (2014), The 2011 Virginia M_w 5.8 earthquake: Insights from seismic reflection imaging into the influence of older structures on eastern U.S. seismicity, *Geol. Soc. Am. Spec. Pap.*, *509*, 285–294.
- Prince, P. S., and J. A. Spotila (2013), Evidence of transient topographic disequilibrium in a landward passive margin river system: Knickpoints and paleo-landscapes of the New River basin, southern Appalachians, *Earth Surf. Processes Landforms*, *38*, 1685–1699.
- Rankin, D. W., W. Dillon, D. Black, S. Boyer, D. Daniels, R. Goldsmith, J. Grow, J. Horton, D. Hutchinson, and K. Klitgord (1991), *Central Kentucky to Carolina Trough*, Geol. Soc. of Am, Boulder, Colo.
- Rhea, S. (1989), Evidence of uplift near Charleston, South Carolina, *Geology*, *17*, 311–315.
- Ritsema, J., H. J. van Heijst, and J. H. Woodhouse (1999), Complex shear wave velocity structure imaged beneath Africa and Iceland, *Science*, *286*, 1925–1928.
- Rogers, J. J. W., and M. Santosh (2002), Configuration of Columbia, a mesoproterozoic supercontinent, *Gondwana Res.*, *5*, 5–22.
- Rogers, J. J. W., and M. Santosh (2003), Supercontinents in Earth history, *Gondwana Res.*, *6*, 357–368.
- Rowley, D. B., A. M. Forte, R. Moucha, J. X. Mitrovica, N. A. Simmons, and S. P. Grand (2013), Dynamic topography change of the eastern United States since 3 million years ago, *Science*, *340*, 1560–1563.
- Ruppel, C., G. Dickens, D. Castellini, W. Gilhooly, and D. Lizarralde (2005), Heat and salt inhibition of gas hydrate formation in the northern Gulf of Mexico, *Geophys. Res. Lett.*, *32*, L04605, doi:10.1029/2004GL021909.
- Rychert, C. A., S. Rondenay, and K. M. Fischer (2007), P -to- S and S -to- P imaging of a sharp lithosphere-asthenosphere boundary beneath eastern North America, *J. Geophys. Res.*, *112*, B08314, doi:10.1029/2006JB004619.
- Saltzer, R. L., and E. D. Humphreys (1997), Upper mantle P wave velocity structure of the eastern Snake River Plain and its relationship to geodynamic models of the region, *J. Geophys. Res.*, *102*, 11,829–11,841, doi:10.1029/97JB00211.
- Schaeffer, A., and S. Lebedev (2014), Imaging the North American continent using waveform inversion of global and USArray data, *Earth Planet. Sci. Lett.*, *402*, 26–41.
- Schmandt, B., and E. Humphreys (2010), Seismic heterogeneity and small-scale convection in the southern California upper mantle, *Geochem. Geophys. Geosyst.*, *11*, Q05004, doi:10.1029/2010GC003042.
- Schmandt, B., and E. Humphreys (2011), Seismically imaged relict slab from the 55 Ma Siletzia accretion to the northwest United States, *Geology*, *39*, 175–178.
- Schmandt, B., and F. C. Lin (2014), P and S wave tomography of the mantle beneath the United States, *Geophys. Res. Lett.*, *41*, 6342–6349, doi:10.1002/2014GL061231.
- Sigloch, K. (2011), Mantle provinces under North America from multifrequency P wave tomography, *Geochem. Geophys. Geosyst.*, *12*, Q02W08, doi:10.1029/2010GC003421.
- Smith, D. L., and W. T. Dees (1982), Heat flow in the gulf coastal plain, *J. Geophys. Res.*, *87*, 7687–7693, doi:10.1029/JB087iB09p07687.
- Soller, D. (1988), Geology and tectonic history of the lower Cape Fear river valley, southeastern North Carolina.
- Spotila, J. A., G. C. Bank, P. W. Reiners, C. W. Naeser, N. D. Naeser, and B. S. Henika (2004), Origin of the Blue Ridge escarpment along the passive margin of Eastern North America, *Basin Res.*, *16*, 41–63.
- Thomas, M. D. (1982), Gravity studies of the Grenville province: Significance for Precambrian plate collision and the origin of anorthosite, in *1982 SEG Annual Meeting*, pp. 109–123, Soc. of Explor. Geophys, Dallas, Tex.
- Thomas, W. A. (2006), Tectonic inheritance at a continental margin, *GSA Today*, *16*, 4–11.
- Thomas, W. A. (2010), Interactions between the southern Appalachian–Ouachita orogenic belt and basement faults in the orogenic footwall and foreland, *Geol. Soc. Am. Mem.*, *206*, 897–916.
- Tuttle, M. P., E. S. Schweig, J. D. Sims, R. H. Lafferty, L. W. Wolf, and M. L. Haynes (2002), The earthquake potential of the New Madrid seismic zone, *Bull. Seismol. Soc. Am.*, *92*, 2080–2089.
- UC San Diego (2013), Central and eastern US network, Int. Fed. of Digital Seismograph Networks, doi:10.7914/SN/N4.
- University of South Carolina (1987), South Carolina Seismic Network, Int. Fed. of Digital Seismograph Networks, doi:10.7914/SN/CO.
- USGS National Earthquake Information Center (NEIC) (1990), United States National Seismic Network, Int. Fed. of Digital Seismograph Networks, doi:10.7914/SN/US.
- Van Arsdale, R. B., and R. T. Cox (2007), The Mississippi's curious origins, *Sci. Am.*, *296*, 76–82.
- Van De Plassche, O., A. J. Wright, B. P. Horton, S. E. Engelhart, A. C. Kemp, D. Mallinson, and R. E. Kopp (2014), Estimating tectonic uplift of the Cape Fear Arch (south-eastern United States) using reconstructions of Holocene relative sea level, *J. Quat. Sci.*, *29*, 749–759.
- Van der Hilst, R., S. Widiyantoro, and E. Engdahl (1997), Evidence for deep mantle circulation from global tomography, *Nature*, *386*, 578–584.
- Van Wijk, J. W., W. S. Baldrige, J. Van Hunen, S. Goes, R. Aster, D. D. Coblenz, S. P. Grand, and J. Ni (2010), Small-scale convection at the edge of the Colorado Plateau: Implications for topography, magmatism, and evolution of Proterozoic lithosphere, *Geology*, *38*(7), 611–614.
- Vlahovic, G., C. A. Powell, M. C. Chapman, and M. S. Sibol (1998), Joint hypocenter-velocity inversion for the eastern Tennessee seismic zone, *J. Geophys. Res.*, *103*, 4879–4896, doi:10.1029/97JB01891.
- Vogt, P. R. (1991), Bermuda and Appalachian-Labrador rises: Common non-hotspot processes?, *Geology*, *19*, 41–44.
- Vogt, P. R., and W.-Y. Jung (2007), Origin of the Bermuda volcanoes and the Bermuda Rise: History, observations, models, and puzzles, *Geol. Soc. Am. Spec. Pap.*, *430*, 553–591.
- Wagner, L. S., K. Stewart, and K. Metcalf (2012), Crustal-scale shortening structures beneath the Blue Ridge Mountains, North Carolina, USA, *Lithosphere*, *4*, 242–256.
- West, J. D., M. J. Fouch, J. B. Roth, and L. T. Elkins-Tanton (2009), Vertical mantle flow associated with a lithospheric drip beneath the Great Basin, *Nat. Geosci.*, *2*, 438–443.
- Wheeler, R. L. (1995), Earthquakes and the cratonward limit of Iapetan faulting in eastern North America, *Geology*, *23*, 105–108.
- Willetts, S. D., S. W. McCoy, J. T. Perron, L. Goren, and C.-Y. Chen (2014), Dynamic reorganization of river basins, *Science*, *343*, 1248765.
- Williams, H., and R. D. Hatcher (1983), Appalachian suspect terranes, *Geol. Soc. Am. Mem.*, *158*, 33–53.

- Winker, C. D., and J. D. Howard (1977), Correlation of tectonically deformed shorelines on the southern Atlantic coastal plain, *Geology*, *5*, 123–127.
- Wolin, E., S. Stein, F. Pazzaglia, A. Meltzer, A. Kafka, and C. Berti (2012), Mineral, Virginia, earthquake illustrates seismicity of a passive-aggressive margin, *Geophys. Res. Lett.*, *39*, L02305, doi:10.1029/2011GL050310.
- Woodward, M. J. (1992), Wave-equation tomography, *Geophysics*, *57*, 15–26.
- Yuan, H., and K. Dueker (2005), Upper mantle tomographic V_p and V_s images of the Rocky Mountains in Wyoming, Colorado and New Mexico: Evidence for a thick heterogeneous chemical lithosphere, in *The Rocky Mountain Region: An Evolving Lithosphere Tectonics, Geochemistry, and Geophysics*, pp. 329–345, AGU, Washington, D. C.
- Yuan, H., and B. Romanowicz (2010), Lithospheric layering in the North American craton, *Nature*, *466*, 1063–1068.
- Yuan, H., S. French, P. Cupillard, and B. Romanowicz (2014), Lithospheric expression of geological units in central and eastern North America from full waveform tomography, *Earth Planet. Sci. Lett.*, *402*, 176–186.
- Zandt, G., H. Gilbert, T. J. Owens, M. Ducea, J. Saleeby, and C. H. Jones (2004), Active foundering of a continental arc root beneath the southern Sierra Nevada in California, *Nature*, *431*, 41–46.
- Zhang, Q., E. Sandvol, and M. Liu (2009), Tomographic P_n velocity and anisotropy structure in the central and eastern United States, *Bull. Seismol. Soc. Am.*, *99*, 422–427.